Modelling Gas-Oil Interactions for Enhanced Oil Recovery: A Numerical and Analytical Study

by

Mohammad Hossein Doranehgard

A thesis submitted in partial fulfillment of the requirements for the degree of

Master of Science

in

Petroleum Engineering

Department of Civil and Environmental Engineering

University of Alberta

© Mohammad Hossein Doranehgard, 2021

Abstract

In the first part of this study, we use an analytical approach and the interpolation-supplemented lattice Boltzmann method (ISLBM) to quantify convective and diffusive transport during CO_2 dissolution in the oil bulk phase. In the first step, we use a turbulence analogy and the ISLBM to determine the relationship between the Rayleigh number (Ra) and the ratio of the pseudo-diffusion coefficient to the molecular diffusion coefficient ($\frac{D^*}{D}$). We then use experimental data from two oil samples, condensate and crude oils, to validate the obtained relationship between $\frac{D^*}{D}$ and Ra. We also use the Sherwood number (Sh), total mixing and diffusive transport curves to analyze different periods during CO_2 dissolution for condensate and crude oils. We focus in particular on how Ra affects the characteristics of density-driven fingers and the convection field. Our results show that there is a logarithmic trend between $\frac{D^*}{D}$ and Ra. Analysis of the total mixing and diffusive curves indicates that the CO_2 dissolution process can be divided into three distinct periods, namely diffusive transport, early convection, and late convection. We find that more than 50% of the ultimate CO_2 dissolution occurs in the early convection period. We also show that the analytical results obtained for the critical time and critical depth at the onset of convection is in good agreement with those of ISLBM. After the onset of convection, the formation of initial fingers leads to enhanced convective transport, with marked implications for the concentration variance and mixing rate.

In the second part of this study, we propose a novel analytical solution to predict the diffusion coefficient and depth of gas (C_1 and a mixture of C_1/C_2 with the molar ratio of 70/30) penetration during the soaking period of the cyclic gas injection process.

Our analytical solution is derived from the modeling of gas-phase pressure declines by use of mass-balance and continuity equations. We model mass transport during the soaking period as a counter-diffusion process, and found that diffusion coefficient and velocity are controlled by the pressure gradient at the early soaking times and the concentration gradient when the soaking progresses. The estimated diffusion coefficients through our solution for a mixture of

gas/oil under tight porous media conditions are in agreement with published literature. We calculate the depth of gas penetration in the plug, and show that the gas front reaches the other end of the plug at the end of the soaking period in the gas-mixture case. Also, the model is capable of predicting swelled oil volume by gas dissolution. A thermodynamic consistency check was performed by comparing the amount of leaked-off gas in the experiment and that of the model. The results show that these values are in the same range.

Preface

Chapter 2 is published in a peer-reviewed journal as "Doranehgard, M. H., & Dehghanpour, H. (2020). Quantification of convective and diffusive transport during CO_2 dissolution in oil: a numerical and analytical study. *Physics of Fluids*, *32* (8), 085110".

Chapter 3 is published in a peer-reviewed journal as "Doranehgard, Mohammad Hossein, Son Tran, and Hassan Dehghanpour. "Modeling of natural-gas diffusion in oil-saturated tight porous media." *Fuel* 300 (2021): 120999".

This thesis is an original work done by Mohammad Hossein Doranehgard.

Dedication

To my parents, brother and sister

Acknowledgments

I would like acknowledge my supervisor, Dr. Hassan Dehghanpour, who admitted me to the research group and supervised me during this project. I cannot imagine getting through this program without his undying support, fascinating research ideas, steady encouragement, and friendship.

I am indebted to the University of Alberta-Future Energy Systems (Project T07-P05) for their financial support.

My appreciation is extended towards my colleagues in the research group (Son Tran, Mahmood Reza Yassin, Ali Habibi, Obinna Ezulike, Yingkun Fu, Amin Alinejad, Mohammad Yousefi, Tamer Moussa, Taregh Soleiman Asl) for their valuable contributions, fruitful discussions, and encouragement.

Table of Contents

List of Tables

List of Figures

Nomenclature

Notations

A = cores surface area, m^2

c = concentration, kg/m^3

$C_\emptyset$ =rock compressibility, $1/pa$

D = diffusion coefficient, m^2/s

D^* = Psudeo- difussion coeficient, m^2/s

k = permeability, m^2

n = number of moles, mole

MW   = molecular weight, g/mol

p = pressure, bar

$\partial p/\partial t$ = pressure drop, Pa/s

$\partial p/\partial x$ = pressure drop, Pa/m

p_{eq} = equilibrium pressure, bar

ΔP_i = initial differential pressure, bar

p_o = oil (pore) pressure, bar

p_g = gas-injection pressure, bar

q = Darcy velocity, m/s

Ra   =Raylegh Number, dimensionless

t = dimensional time, hours

u = velocity, m/s

α = dimensionless number defined in Eq. (3-7)

η = Similarity variable in Eq. (B-5)

μ = viscosity, Pa.s

ξ =mixing rate, dimensionless

ρ_s = density of solvent, kg/m^3

ρ_o = density of oil, kg/m^3

$\sigma^2(\tau)$ =Concentration varience, dimensionless

τ =dimensionless time, dimensionless

$\emptyset$ = porosity, dimensionless

ω_s = mass fraction of component i in j phase, dimensionless

ω_{so} = saturation of mass fraction of component i in j phase, dimensionless

Subscripts

abs   = absolute

atm   = atmosphere

eq   = equilibrium

f   = final

g   = gas

i   = initial

o   = oil

Acronyms

AARD   = average absolute relative deviation, dimensionless

EOR   = enhanced oil recovery

EOS   = equation of state

HnP   = huff 'n' puff

ISLBM   = interpolation-supplemented lattice Boltzmann method

LBM   = lattice Boltzmann method

MMP   = minimum miscibility pressure

PR-EOS = Peng-Robinson equation of state

Chapter 1 : Introduction

1.1.Background

International Energy Outlook 2020 (Briefing, 2020) predicts that that the global consumption of energy increases 50% by 2050. In this report, by 2050, petroleum and other liquids will contribute in the total energy sources with a share of 25% (Briefing, 2020). Unconventional petroleum resources cover around 80% of the total petroleum sources in the world (Zou, 2017). At this point, gas and oil recovery from the unconventional sources plays a key role in responding to the ever-increasing demand for energy. The recovery factor of the tight and shale formations, however, after injecting billion barrels of facing fluids (Figure 1–1), is less than 10% of the original oil in place (Hughes, 2013; Sheng, 2015). In this regard, using enhanced oil recovery (EOR) methods in these formations seems to be necessary.
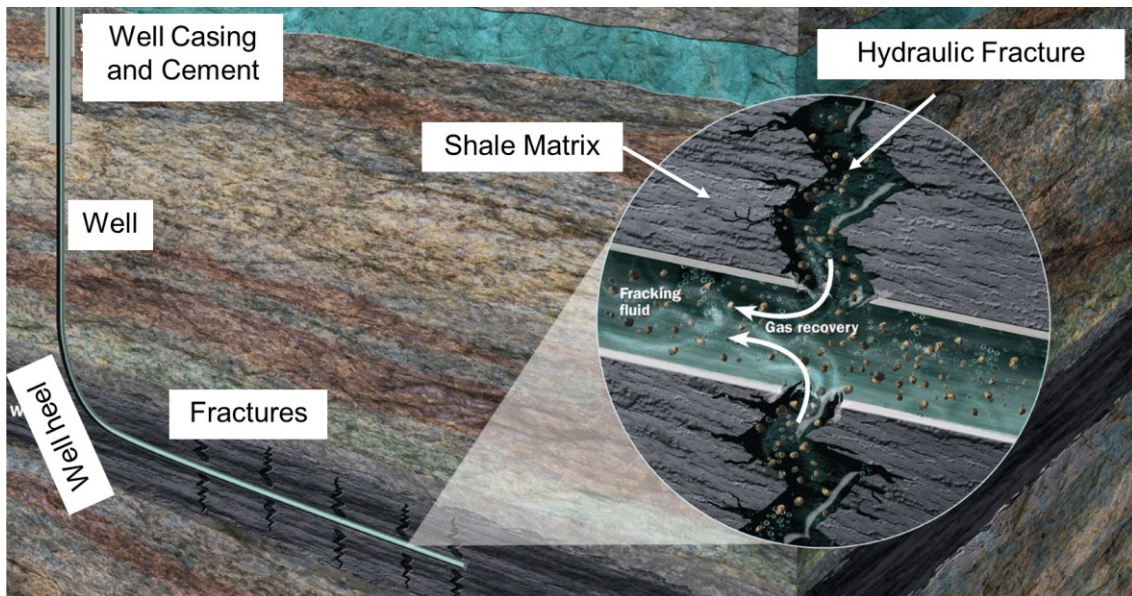
Figure 1–1: Recovery factor of tight and shale formations is less than 10% of original oil in place after hydraulic fracturing (Yassin, 2019).

Nowadays, gas-EOR methods lie in the interest of industries and researchers owning to their acceptable efficiency and environmental pollution degradation impacts (Huang et al., 2019; Kumar and Mandal, 2017). For tight and shale formations with ultra-low permeability, gas (CO_2, C_1, C_2) Huff-n-Puff method excels in comparison to the conventional gas-injection technique (Carpenter, C., 2018; Thakur, 2019). Generally, Gas HnP method includes three steps: (i) gas injection, (ii) soaking period during which the well is shut-in, (iii) puff or production period. Figure 1–2 (Yassin, 2019) depicts deferent steps of CO_2 HnP in a tight formation. In the huff-n-puff process, molecular diffusion which is a slow mechanism is responsible for gas dissipation into the low-permeability formation (Tran et al. 2021). An important parameter in the molecular diffusion process is diffusion coefficient (D).
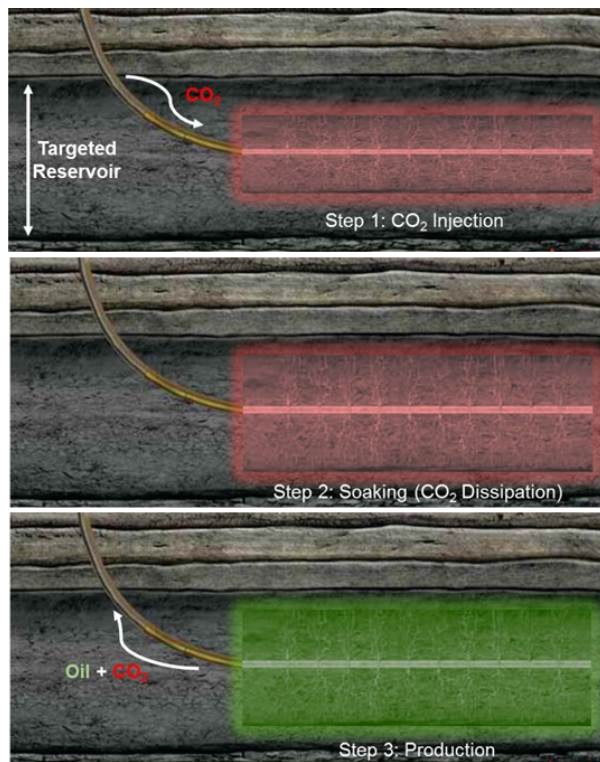
Figure 1–2: Schematic illustration of CO_2-transport and oil-recovery mechanisms during the gas HnP process (Yassin, 2019).

Most researchers typically conduct bulk-phase gas/oil experiments to estimate diffusion coefficient. This experiment is comprised of pressure buildup (gas injection) and soaking steps. The pressure data during the soaking process are then analyzed to estimate the diffusion coefficient (Guo et al., 2009; Janiga et al., 2020; Li et al., 2017; Sadegh Sharafi et al., 2020; Zhang, Y.P. et al., 2000; Zheng et al., 2016a; Zheng et al., 2016b). In these research studies, the researchers assumed that there is no convection field within the bulk phase. However, by CO_2 dissolution into oil and water, the mixture's density increases that may cause introducing density-driven fingers and subsequent convection field within the liquid bulk phase (Farajzadeh et al., 2007). In this content, Yassin et al. (2018) used a light oil sample and CO_2 to conduct a bulk-phase experiment by using a custom-designed visual cell. They visually observed density-driven fingers that act as the convection mechanisms and significantly increase the CO_2 dissolution rate into the oil phase. Therefore, when we are using CO_2 as the injected gas, it is important to calculate the molecular diffusion coefficient properly in the presence of a (possible) convection field.

Besides the bulk phase studies, as we deal with the tight formations in HnP process, it is necessary to calculate the value of diffusion coefficient in the core-scale. Most researchers used different tortuosity models and numerical simulation methods to convert the calculated value of diffusion coefficient in the bulk phase to that of core-scale (Kerr et al., 2020; Li et al., 2018b; Lou et al., 2019; Schopper, 1966). However, the diffusion coefficients estimated using these methods have significant errors due to the uncertainties involved in quantifying the tortuosity factor (Moldrup et al., 2004). Therefore, the lack of a robust analytical model for calculating diffusion coefficient in core-scale is obvious.

1.2.Research objectives

In the first part of this research, we investigate the gas-oil interactions in the bulk phase. In this content, we first introduce the governing equations and statistical variables, followed by their physical description. Using ISLBM and the turbulence analogy, we investigate the ratio of the pseudo diffusion coefficient (representing convective transport) to the diffusion coefficient (representing diffusive transport). Then, we use experimental data from two oil

samples to investigate the different periods and their characteristics during CO_2 dissolution. After that, we use an analytical approach and scaling analysis to investigate the time and depth at the onset of convection. Finally, we investigate the effects of the Rayleigh number on the density-driven fingers, mixing rate, dominant physics (diffusive or convective transport) and the finger length.

In the next part, we investigate the gas-oil interactions in the pore-scale. In this regard, we propose a novel analytical solution to quantify the diffusion coefficient, oil recovery, and pressure profile along the core plug during the soaking period of the gas HnP process. First, we model the mass-transport process using pressure-declined data, mass-balance, and continuity equations. Second, the model is verified against experimental data previously published (Tran et al., 2021). Next, we use the calibrated model to determine the depth of gas penetration, gas concentration, velocity, and pressure profiles along the plug. Moreover, the effect of injection-gas enrichment (by C_2 in this study) on transport properties are also investigated.

1.3.Dissertation outlines

The dissertation is divided into 4 chapters. Chapters 2 and 3 are published as peer-reviewed journal papers.

Chapter 1 presents the background, objectives of the research, and the dissertation outline.

Chapter 2 investigates diffusive and convective transport during CO_2 dissolution in condensate and crude oils. In this part we investigate the effects of convection field on the calculated value of the diffusion coefficient.

Chapter 3 provides a novel model to calculate the diffusion coefficient in the core-scale. In this chapter, we study gas-front penetration in the tight core plug as well as the amount of oil recovery during the soaking period.

Chapter 4 includes the conclusions of the previous chapters as well as some recommendations for the future works.

Chapter 2 : CO$_2$ dissolution in oil bulk phase

This chapter investigates CO$_2$ dissolution process in oil using pseudo-diffusion coefficient, dimensionless numbers and statistical parameters including mixing rate and concentration variance.

2.1.Introduction

CO$_2$ dissolution in liquids, such as saline water and different types of oils, has been gaining attention owing to its importance in petroleum and environmental engineering (Damen et al., 2005; Song and Yang, 2017). Enhanced oil recovery using the huff-n-puff method and CO$_2$ injection into geological formations are just some notable examples (Li et al., 2018a; Mohagheghian et al., 2019; Vilarrasa et al., 2010).

When CO$_2$ is dissolved into oil and water, the density of the solution increases relative to that of the baseline liquid (Ashcroft and Isa, 1997; Haas et al., 1973). On initial injection, CO$_2$ is dissolved at the gas-liquid interface via molecular diffusion (Lindeberg and Wessel-Berg, 1997). Therefore, the density at the CO$_2$-liquid interface increases, causing the interface to become unstable. This instability produces natural convection in the liquid phase, enhancing CO$_2$ mass transfer (Farajzadeh et al., 2007; Yang and Gu, 2006). In this context, owing to the presence of a convection field, Fick's law cannot mathematically model the dissolution process.

Researchers have investigated the existence of natural convection due to CO$_2$ dissolution into oil and water. Lindeberg and Bergmo (2003) investigated the fate of CO$_2$ injected into a sealed aquifer with different permeabilities. They found that the long-term fate of dissolved CO$_2$ in the aquifers is controlled by the resultant convection field. Hassanzadeh et al. (2006; 2005) numerically studied the convection field in geological CO$_2$ storage. Their results show that in choosing aquifers for CO$_2$ storage, the existence and strength of convective instability is important. Rapaka et al. (2008) investigated the governing equations in a 3-D space for geologic sequestration of CO$_2$ using non-modal stability theory. They proved that the time at which convection begins strongly depends on the size of the

perturbations. Zhang et al. (2007) developed a parallel numerical code to simulate CO_2 sequestration in geological saline aquifers. Lu and Litchtner (2007) used a 3-D parallel code to study the effects of Reynolds instabilities on supercritical CO_2 dissolution in saline aquifers. They concluded that owing to density-driven instabilities, the simulated CO_2 dissolution rate is a strong function of the grid resolution. Nazari Moghaddam et al. (2012) evaluated the pseudo-diffusion coefficient (D^*) of CO_2 injection into water using pressure decay theory. Their results reveal that (i) the extracted value of D^* is higher than the molecular diffusion of CO_2 in water (ii) D^* is a key parameter in the CO_2 sequestration process. Nevertheless, the relation between $\frac{D^*}{D}$ and Ra as well as different periods during CO_2 dissolution has yet to be fully understood.

To date, researchers have implemented various numerical methods to simulate transport processes such as heat transfer and fluid flow (Karimi et al., 2016; Xiong et al., 2020b). One such method is the Lattice Boltzmann Method (LBM). Based on molecular theory, LBM can simulate physical phenomena with complex geometries (Guo and Shu, 2013). During the last decade, LBM has been used to simulate various fluid flow and heat-transfer phenomena (Ahangar et al., 2020; NingguangChen et al., 2020). Kefayati (2020) used an immersed boundary-lattice Boltzmann method to study natural and mixed convection in the cavities with complex geometries. He showed that the proposed LBM can simulate heat transfer process with enough accuracy. Kalteh and Hasani (2014) used LBM to study free convection in a L-shape cavity containing a nanofluid. Ghassemi and Siavashi (2017) used the parallel LBM to study heat transfer and entropy generation in a cavity with a linear distribution of temperature on the side walls. As the origin of the driving force in both heat transfer by convection and the density-driven fingers in the CO_2 dissolution process is density difference, using LBM in this study is viable.

Nevertheless, researchers implement modifications on the lattice Boltzmann method due to the existence of instabilities in the simulation domain (i.e. eddies, boundary layers). These modifications on LBM enable the researchers to simulate different problems with acceptable precision and lower computational cost. Jami et al. (2016) used a multiple-relaxation-time (MRT) LBM to investigate the heat transfer in a 2-D square cavity. They

observed that MRT- LBM shows a good performance for capturing laminar and transient flow features. Kuznik et al. (2007) applied Taylor series expansion – and least square – based lattice Boltzmann method (TLLBM) to investigate the laminar and transient natural convection. They used a non-uniform mesh to capture the instabilities with a reasonable computational cost. Vishnampet et al. (2011) used interpolation supplemented LBM (ISLBM) to investigate the natural convection inside a 2-D porous enclosure at high Rayleigh numbers. They observed a good match between their results with those of previous research works. Dixit and Babu (2006) utilized ISLBM to investigate heat transfer by natural convection in a square cavity. They concluded that ISLBM is properly able to capture the velocity and temperature gradients.

In this study, we first introduce the governing equations and statistical variables, followed by their physical description. Using ISLBM and the turbulence analogy, we investigate the ratio of the pseudo diffusion coefficient (representing convective transport) to the diffusion coefficient (representing diffusive transport). Then, we use experimental data from two oil samples to investigate the different periods and their characteristics during CO_2 dissolution. After that, we use an analytical approach and scaling analysis to investigate the time and depth at the onset of convection. Finally, we investigate the effects of the Rayleigh number on the density-driven fingers, mixing rate, dominant physics (diffusive or convective transport) and the finger length.

2.2. Problem definition

2.2.1. Experimental observations and pressure-decline data

Here we present experimental observations and pressure-decline curves for CO_2 dissolution in condensate and crude oils with the physical properties listed in Table 2–1. The aim is to present the problem and our approach for solving it using pressure-decline data and LBM. In this context, Yassin et al. (2018) experimentally investigated the CO_2 dissolution process in condensate and crude oils using a visual cell setup (Yassin et al., 2018). Figure 2–1 shows their observations for CO_2 dissolution into condensate oil. It can be seen that as time progresses, the dissolved CO_2 produces density-driven fingers as well as a convection field within the oil phase. In addition, as the CO_2 concentration in the oil

7

phase increases, the mixture moves to the bottom of the cell, consistent with the fact that the oil density increases with CO_2 dissolution.

Table 2–1: Physical properties of condensate and crude oils at 50 ^{0}C (Santos et al., 2017; Yassin et al., 2018).

Oil type	Viscosity (cp) @ Average pressure	Density (kg/m³) @ Atmospheric pressure	Δρ (kg/m³) @ Maximum pressure difference	MW (g/mol)
Condensate oil	1.6	787	15	148.03
Crude oil	6	835	10	251.78
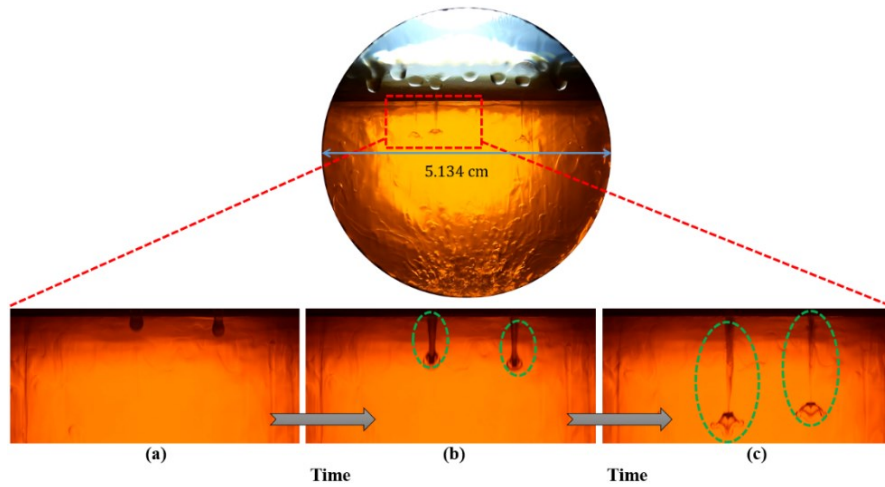
Figure 2–1: Experimental observations of CO_2 dissolution in a light oil (modified from Yassin et al. (2018)).

Figure 2–2 (Yassin et al., 2018) shows the pressure-decline curves of this experiment that consists of region1 and region 2. Region 1 has a steeper pressure-decline slope than region 2. Our hypothesis is that regions 1 and 2 are controlled by convective and diffusive transport, respectively. In fact, we believe that, for the first region, an appropriate value of the diffusion coefficient (i.e. the pseudo-diffusion coefficient) should be used. We assume that there should be a relationship between Ra and the ratio of the pseudo-diffusion

coefficient (D*) and molecular diffusion. To test our hypothesis, we perform calculations using the pressure-decline data of Figure 2–2. Figure 2–3 shows ln $(p - p_{eq})$ as a function of time. It can be seen that for condensate and crude oils, the slope of region 1 is, respectively, 14.61 and 8.11 times higher than that of region 2.

Using Zhang's model (2000) and k-means data clustering method (Berkhin, 2006) in region 2 (diffusion dominated), we find that the diffusion coefficient for the CO_2 and condensate oil sample is around 5×10^{-9} m²/s. This value for the CO_2 and crude oil sample is almost equal to 6×10^{-9} m²/s. Consequently, the associated Ra values for condensate and crude oils are around 1.84×10^7 and 2.725×10^6, respectively.

Next, we test our hypothesis and investigate the relationship between Ra and the ratio of the pseudo-diffusion coefficient and molecular diffusion $(\frac{D^*}{D})$. We also calculate the onset of convection as well as the share of convection and molecular diffusion in the CO_2 dissolution process for the condensate and crude oils.

(a)

(b)
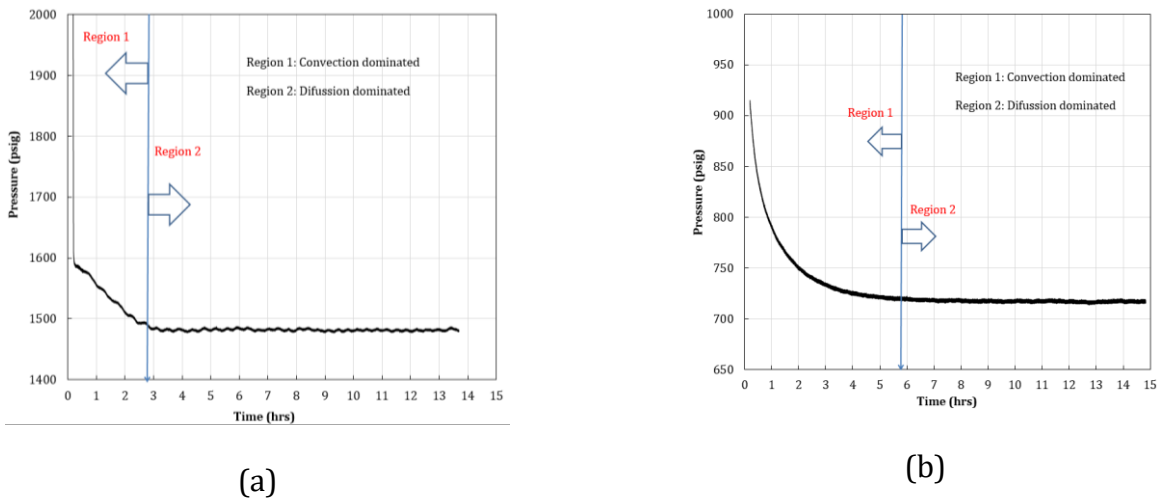
Figure 2–2: Pressure-decline curve versus time for (a) condensate and (b) crude oils. Two regions, convection dominated and diffusion dominated, are observed.
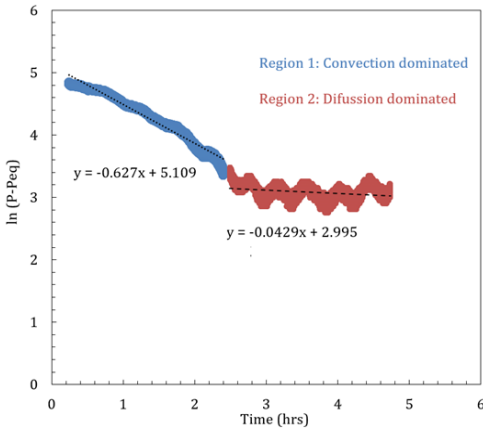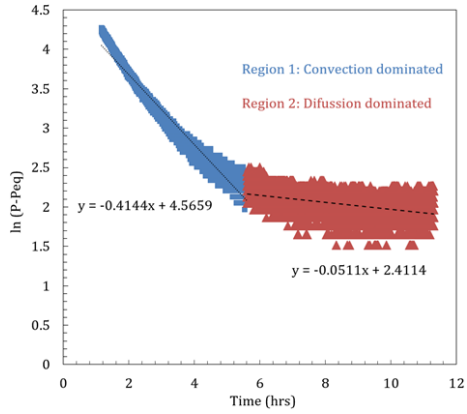
Figure 2–3: Plot of $\ln(p - p_{eq})$ versus time for (a) condensate and (b) crude oils. Using Zhang's model, the diffusion coefficient for two different regions can be calculated.

2.2.2.Physical description of the computational domain

To investigate our hypothesis, we should define a computation domain. In our computational domain, CO_2 is continuously in contact with the top side of a 2-D square whose sides are 0.01 m in length, as shown in Figure 2–4. At t=0, the CO_2 concentration in the oil phase is zero. We assume that the side and bottom walls are impermeable. There is no heat transfer, and the temperature is set at 50 ºC that remains constant. The velocity on all walls is zero (no slip conditions).
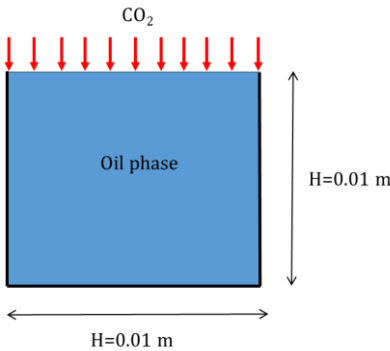
Figure 2–4: Physical description of the problem. For simplicity, we consider a 2-D square shape for the computational domain.

2.3. Mathematical modeling

2.3.1. Governing equations

To model CO_2 dissolution in oil, the non-dimensional continuity, x-momentum, y-momentum, and convection-diffusion equations are solved (for the momentum equations, we ignore the inertia effects) (Khosrokhavar, 2015; Siavashi et al., 2015; Yaghoubi Emami et al., 2018):

$$\frac{\partial \bar{\rho}}{\partial \tau} + \frac{\partial (\bar{\rho}U)}{\partial X} + \frac{\partial (\bar{\rho}V)}{\partial Y} = 0 \tag{2-1}$$

$$\frac{\partial U}{\partial \tau} + \left(U\frac{\partial U}{\partial X} + V\frac{\partial U}{\partial Y} \right) = -\frac{\partial \bar{p}}{\partial X} \tag{2-2}$$

$$\frac{\partial V}{\partial \tau} + \left(U\frac{\partial V}{\partial X} + V\frac{\partial V}{\partial Y} \right) = -\frac{\partial \bar{p}}{\partial Y} - Ra\,Sc\,C \tag{2-3}$$

$$\frac{\partial C}{\partial \tau} + U\frac{\partial C}{\partial X} + V\frac{\partial C}{\partial Y} = \frac{1}{Ra}(\frac{\partial^2 C}{\partial X^2} + \frac{\partial^2 C}{\partial Y^2}) \tag{2-4}$$

In the above equations, the dimensionless variables are defined as follows (Izadi et al., 2020; Yaghoubi Emami et al., 2018):

$$\tau = \frac{D}{H^2}t, X = \frac{x}{H}, Y = \frac{y}{H}, \bar{\rho} = \frac{\rho}{\rho_0}, U = \frac{uH}{D}, V = \frac{vH}{D}, \bar{p} = \frac{pH^2}{\rho_0 D^2}, C = \frac{c - c_i}{c_0 - c_i} \tag{2-5}$$

In addition, using analogy from the heat transfer, the Schmitt (Sc) and Rayleigh (Ra) numbers are defined as (Satbhai and Roy, 2020):

$$Sc = \frac{v}{D}, Ra = \frac{g(\beta \Delta c)\,H^3}{Dv} \tag{2-6}$$

The mixture density (ρ) is defined via the Boussinesq approximation (Guerrero-Martínez et al., 2017):

$$\rho = \rho_0(1 + \beta(c - c_0)) \tag{2-7}$$

The degree of mixing is defined as:

$$\xi = 1 - \frac{\sigma^2(\tau)}{\sigma_{max}^2} \tag{2-8}$$

where $\sigma^2(\tau)$ is defined by (Fattahi et al., 2017; Jha et al., 2011)

$$\sigma^2(\tau) = \overline{c^2} - \bar{c}^{\,2} = \overline{(c - \bar{c})^2} \tag{2-9}$$

Here, "$\bar{\cdot}$" represents spatial averaging over the domain. In fact, when $\sigma(t)^2 = 1$ ($\xi = 0$), the mixture is fully segregated. However, when $\sigma(t)^2 = 0$ ($\xi = 0$), the mixture is perfectly mixed.

The Taylor microscale (dissipation scale), where the fluctuations are affected by diffusion, is defined by

$$s = \sqrt{\frac{\sigma^2(\tau)}{\epsilon Ra}} \tag{2-10}$$

Here ϵ is the dimensionless dissipation rate defined by (Jha et al., 2011)

$$\epsilon = \frac{\overline{|\nabla C|^2}}{Ra} \tag{2-11}$$

Multiplying Eq. (2-4) by C and averaging over the domain, we obtain (Jha et al., 2011)

$$\frac{d\sigma^2(\tau)}{d\tau} = 2\,\epsilon \tag{2-12}$$

where ϵ can be expressed as the mixing rate or the rate at which the fluctuations are dispatched (Jha et al., 2011).

2.4. Results and discussion

Here we present the results in five subsections. First, by using the turbulence analogy, we find $\frac{D^*}{D}$ at each value of Ra. Second, using experimental data from the two oil samples, we investigate different periods during CO_2 dissolution. Third, we investigate the critical time and the position of transient Ra (critical depth) at the onset of convection using an analytical approach and compare the results with numerical simulations (ISLBM). Fourth, we perform

a scaling analysis at the onset of convection. Fifth, we study the effect of Ra on the fingering phenomenon at different times in terms of the concentration variation (σ^2), mixing rate (ϵ), iso-concentration and finger length.

2.4.1. Molecular diffusion coefficient and mixing

Here we use the turbulence analogy to estimate D* corresponding to the combined effects of diffusive and convective transport within the oil phase. In addition, we decouple D* and D to compare the effects of convection and diffusion on the CO_2 dissolution process. The velocity and CO_2 concentration can be written as (Ghorbani et al., 2017; Jha et al., 2011)

$$\begin{cases} u_j = \bar{u}_j + \acute{u}_j \\ c = \bar{c} + \acute{c} \end{cases} \tag{2-13}$$

Here, $\bar{u}_j$ and $\bar{c}$ represent the spatially-averaged velocity and concentration. $\acute{u}_j$ and $\acute{c}$ denote their deviations from the mean values.

Substituting Eq. (2-13) into the convection-diffusion equation yields

$$\frac{d\bar{c}}{dt} + \bar{u}_j\,\overline{\frac{dc}{dx_j}} = D\frac{\partial^2 \bar{c}}{\partial x_j^2} - \frac{\partial}{\partial x_j}\overline{\acute{u}_j\acute{c}} \tag{2-14}$$

Here, $\frac{\partial}{\partial x_j}\overline{\acute{u}_j\acute{c}}$ corresponds to the transport of CO_2 by turbulent fluctuations (Csanady, 2012; Xiong et al., 2020a). The eddy diffusivity coefficient, ε_j, is defined by

$$\overline{\acute{u}_j\acute{c}} = -\varepsilon_j\frac{d\bar{c}}{dx} \tag{2-15}$$

Since ε_j does not depend on the direction, we assume $\varepsilon_x = \varepsilon_y = \varepsilon$ and $\frac{\partial}{\partial x_j}\varepsilon_j = 0$. Therefore, Eq. (2-14) can be written as

$$\frac{d\bar{c}}{dt} + \bar{u}_j\,\overline{\frac{dc}{dx_j}} = (D + \varepsilon)\frac{\partial^2 \bar{c}}{\partial x_j^2} \tag{2-16}$$

$$\frac{\frac{d\bar{c}}{dt} + \bar{u}_j\,\overline{\frac{dc}{dx_j}}}{\frac{\partial^2 \bar{c}}{\partial x_j^2}} = (D + \varepsilon) = D^* \tag{2-17}$$

13

Using Eq. (2-17) and ISLBM, we plot $\frac{D^*}{D}$ versus different values of Ra (Figure 2–5). This figure shows that $\frac{D^*}{D} \propto \ln(\text{Ra})$.
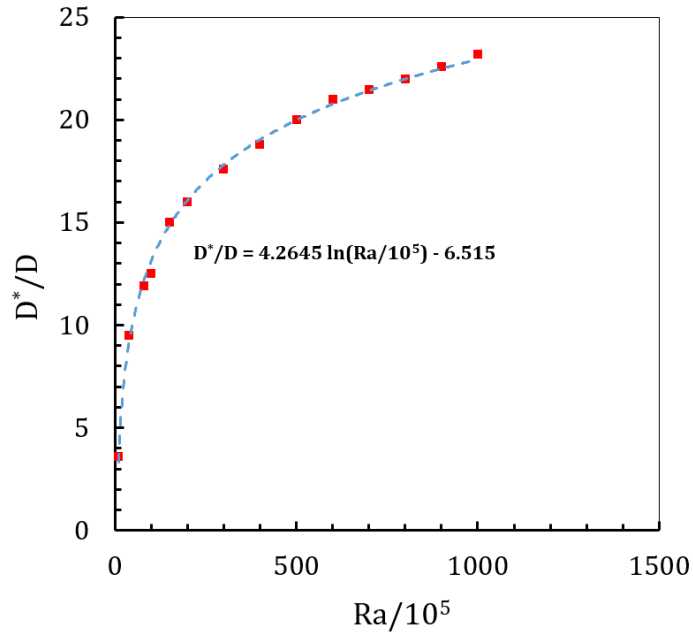
Figure 2–5: Plot of the ratio of pseudo diffusion coefficient to the diffusion coefficient ($\frac{D^*}{D}$) versus Ra

To analyze the observed trend between $\frac{D^*}{D}$ and Ra, we used the data provided in Section 2.2.1. Table 2–2 shows a good agreement between the $\frac{D^*}{D}$ values obtained by (i) pressure-decline data (Figure 2–3) and (ii) the turbulence analogy (Figure 2–5). Therefore, the relationship obtained in Figure 2–5 can be considered valid, providing credence to our hypothesis regarding the relationship between Ra and $\frac{D^*}{D}$.

Table 2–2: Comparing $\frac{D^*}{D}$ values obtained by pressure-decline data and the turbulence analogy.

Oil type	Ra number	$\frac{D^*}{D}$ using pressure decline data (Figure 2–3)	$\frac{D^*}{D}$ using turbulence analogy and LBM (Figure 2–5)	Error
Condensate oil	1.84×10^7	14.61	15.72	7.6%
Crude oil	2.72×10^6	8.11	7.58	6.5%

2.4.2. Mixing regimes and mechanisms

Next we investigate the mixing regimes and the associated mass transfer during CO_2 dissolution in condensate and crude oils. Our hypothesis is that convective mixing plays a central role in the dissolution process. Nevertheless, to quantify the contribution of convective mixing in the dissolution process, we use numerical simulations (ISLBM) and the Sherwood number (Sh) representing the ratio of total mixing to the mixing due to pure diffusion.

Figure 2–6 shows the fraction of ultimate dissolution and Sh as a function of dimensionless time for (a) condensate and (b) crude oils. For condensate and crude oils, more than 60% and 50% of ultimate dissolution occurs within 500s. During this time, molecular diffusion contributes to the dissolution process for almost 30% and 39% for condensate and crude oils, respectively. Figure 2–6 indicates that the share of convective transport for condensate oil is almost 1.4 times higher than that for crude oil. This observation is consistent with the existence of heaver components in crude oil and the higher Ra of condensate oil. In Figure 2–6, we can see that as time progresses, the role of convection increases and then decreases, consistent with the experimental results (Figure 2–2).

To investigate the dissolution mechanisms at earlier times, we show a close-up view of Figure 2–6 in Figure 2–7. By comparing the total mixing curve with the diffusive transport curve, we can identify three distinct periods, namely periods A, B and C, representing

diffusive transport, early convective mixing and late convective mixing, respectively (Hassanzadeh et al., 2007).

In period A, molecular diffusion is the dominant mechanism. During period A, δ_D (penetration depth) and J (mass transferred) $\propto \sqrt{\tau}$ (Einstein, 1905; Hassanzadeh et al., 2007). The duration of this period depends on Ra such that a lower Ra (higher D) corresponds to a longer period. As Ra $_{\text{crude oil}} <$ Ra $_{\text{condensate oil}}$, the duration of period A for crude oil is almost three times longer. This period continues until the onset of convection, which is shown as the separation point in Figure 2–7. Sh = 1 during this period (Hassanzadeh et al., 2007).

At the onset of convection and subsequent instabilities, the separation point arises, marking the start of period B. During this period, by drawing a tangent line on the curve at the separation point, we observe $dc \propto \tau$ (Hassanzadeh et al., 2007). In other words, $\frac{dc}{d\tau} \propto Ra$ and is independent of time. This period continues until the effects of instabilities reach the bottom boundary. Figure 2–7 shows that period B for crude oil is almost two times longer than that for condensate oil due to the lower Ra and weaker convection for the case of crude oil. During this period, Sh increases and reaches a maximum. For condensate and crude oils, period B is responsible for more than 60% and 50% of ultimate dissolution of CO_2, respectively.

As the effects of the bottom boundary layer become important, the total mixing curve deviates from a straight line, marking the start of period C (Hassanzadeh et al., 2007). During this period, Sh starts to decrease and subsequently, the share of convective transport decreases as well. In fact, diminishing density gradients leads to a decreasing velocity field and a lower rate of CO_2 dissolution.
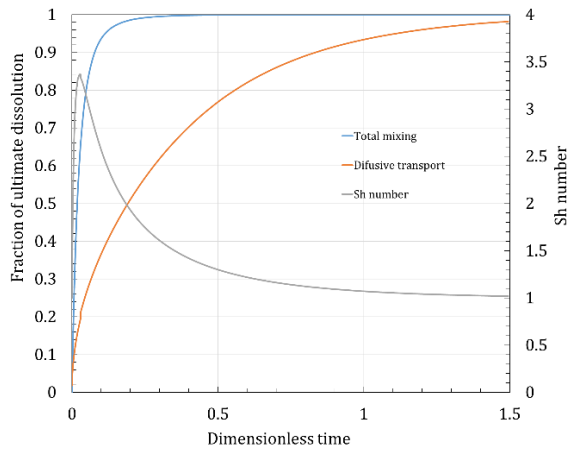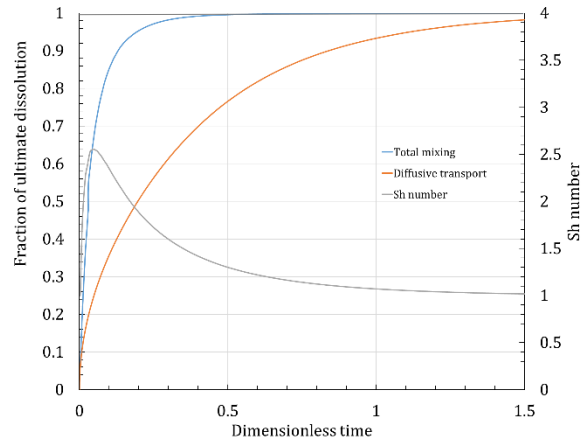
Figure 2–6: Fraction of ultimate dissolution and Sh versus dimensionless time for (a) condensate and (b) crude oils. The Sh number is almost 1.3 higher for condensate oil.
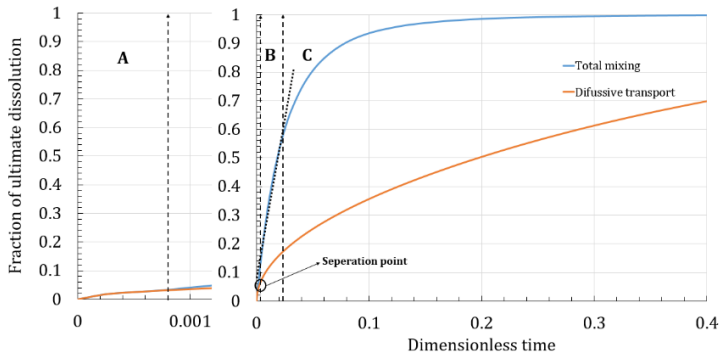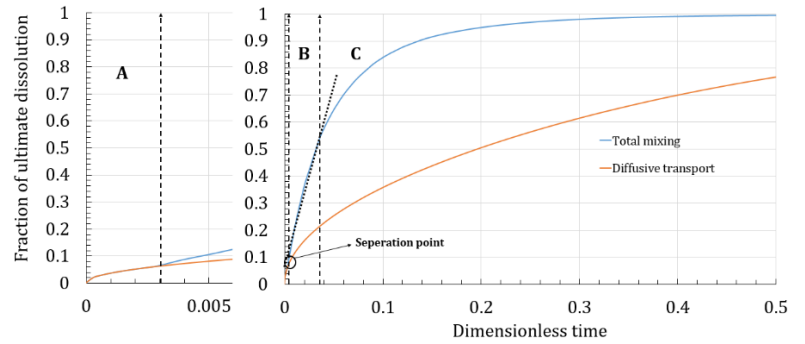
Figure 2–7: Three different regions identified during CO_2 dissolution for (a) condensate and (b) crude oils. In the first period, molecular diffusion dominates. In the second period, $\frac{dc}{d\tau} \propto Ra$. In the third period, the role of convective transport weakens.

2.4.3. Onset of convection

We now determine the time for the onset of convection (t_c) using an analytical method. Our hypothesis is that t_c depends on the system and oil's parameters. Also, the derived value of t_c should be consistent with the experimental data and simulation results.

Here, we define the local (transient) Ra as (Tan et al., 2003b)

$$Ra = \frac{y^4 \Delta \rho \; g}{\mu \; D} \frac{\partial C}{\partial y} \tag{2-18}$$

For the system shown in Figure 2–4, the following boundary conditions are imposed:

$$\begin{cases} C(0,t) = C_{eq} \\ C(\infty, t) = 0 \\ C(y,0) = 0 \end{cases} \tag{2-19}$$

Here, Ceq represents the concentration of CO_2 at the gas/oil interface and at equilibrium pressure (P_{eq}). For the above boundary conditions, the solution of Fick's second law is (Tan et al., 2003a):

$$C\,(y,t) = C_{eq} \; erfc \; (\frac{y}{2\sqrt{Dt}}) \tag{2-20}$$

According to Eq. (2-18), the transient (local) Ra can be written as (Tan et al., 2003a)

$$Ra = \frac{y^4 \Delta \rho \; g}{\mu \; D} \left(\frac{1}{\sqrt{\pi Dt}} \right) exp(-\frac{y^2}{4Dt}) \tag{2-21}$$

By differentiating Eq. (2-21), the maximum transient Ra can be found by solving

$$\frac{\partial Ra}{\partial y} = [4y^3 \; exp\left(-\frac{y^2}{4Dt}\right) + \left(-\frac{2y}{4Dt}\right) y^4 \; exp\left(-\frac{y^2}{4Dt}\right)] = 0 \tag{2-22}$$

That gives y_{max} (critical depth) where the onset of convection occurs:

$$y_{max} = \sqrt{8 \, Dt_c} \tag{2-23}$$

Substituting Eq. (2-23) into Eq. (2-21) gives the maximum value of Ra at the onset of convection:

$$Ra_{max} = \frac{64 \, D \, t_c^2 \, \Delta\rho \, g}{\mu \, e^2 \, \sqrt{\pi \, D \, t_c}} \tag{2-24}$$

Here, the onset of instability at t_c and subsequent convection can be estimated using the critical Ra value (Ra_c) based on Rayleigh-Benard instability (Drazin, 2002). Drazin (Drazin, 2002) estimates $Ra_c \sim 1708$ based on Rayleigh-Benard instability within the liquid bulk phase. Substituting Ra_{max}=1708 into Eq. (2-24) and simplifying it, gives

$$t_c = 10.827 \left(\frac{\mu}{\sqrt{D} \, \Delta\rho} \right)^{\frac{1}{1.5}} \tag{2-25}$$

Using the experimental data provided in the previous section, we can estimate the onset of instability and subsequent convective flow. Table 2–3 lists the critical time, dimensionless time and critical depth at the onset of convection for condensate and crude oils. For crude oil, the critical time and critical depth at the onset of convection are almost three and two times higher than those for condensate oil, respectively.

Table 2–3: Values of Ra, critical time, dimensionless time and critical depth at onset of convection for condensate and crude oils.

Oil type	Ra number	t_c (s)	τ	y_c (mm)
Condensate oil	1.84×10^7	14.24	7.12×10^{-4}	0.754
Crude oil	2.725×10^6	42.38	2.54×10^{-3}	1.426

To evaluate the obtained values for y_c, we use numerical simulations using LBM. Figure 2–8 shows the y_c values at the onset of convection for condensate and crude oils. Figure 2–8 and Table 2–3 show that the analytical results reasonably agree with numerical results for the critical depth (y_c) at the onset of convection.

$t_c= 14.24$ s $y_c=0.761$ mm $t_c= 42.38$ s $y_c=1.386$ mm

(a)   (b)
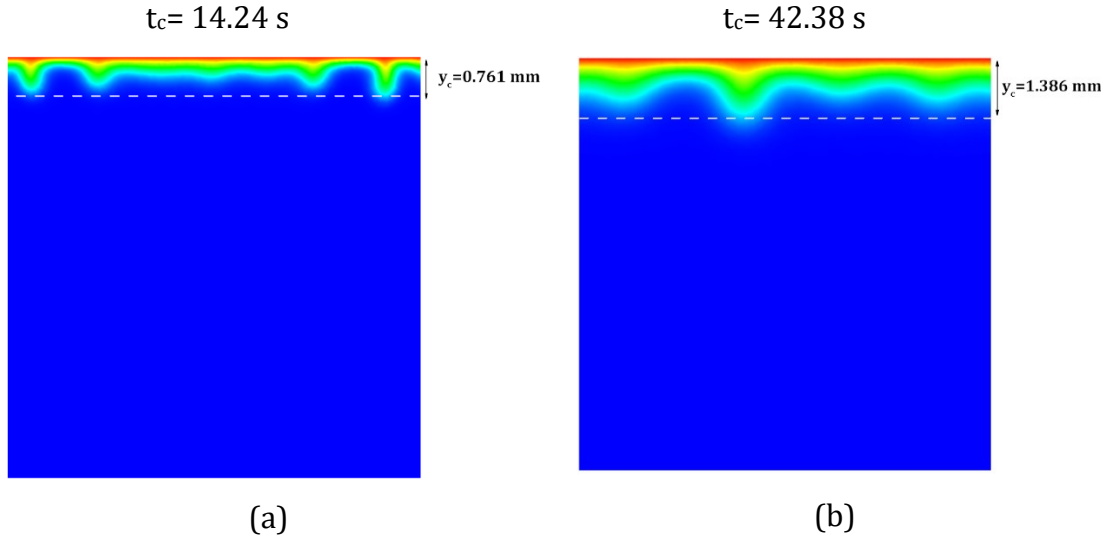
Figure 2–8: The critical depth (y_c) at the onset of convection for (a) condensate and (b) crude oils.

By differentiating Eq. (2-23), the velocity of the introduced fingers at the onset of convection can be calculated by

$$\frac{\partial y}{\partial t} = \sqrt{\frac{2D}{t}} = \frac{D}{H}\sqrt{\frac{2}{\tau}} \tag{2-26}$$

Since the order of magnitude of D, H and τ are O (10^{-9}), O (10^{-2}) and O (10^{-4}), respectively, the approximate velocity of the fingers at the onset of convection is on the order of O (10^{-5}). To evaluate the obtained order of magnitude for the velocity, we plot the velocity versus dimensionless time for different values of Ra in Figure 2–9 using the LBM simulation results. At the onset of convection, we observe good agreement between the analytical and numerical results. Moreover, for Ra>10^5 and τ>0.002, the velocity plateaus owing to effective mixing of the mixture. Nevertheless, some fluctuations in the velocity curves can still be detected. These fluctuations are due to the formation of new fingers. Afterwards, such newly formed fingers are dispersed by molecular diffusion, which causes the velocity to decrease accordingly.
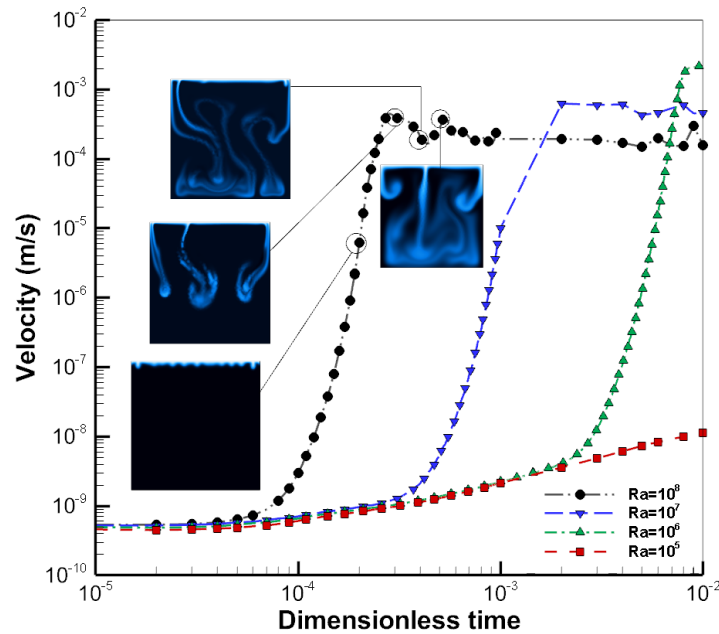
Figure 2–9: Velocity magnitude versus dimensionless time for different values of Ra.

2.4.4. Scaling analysis at the onset of convection

Here, we determine O(Ra) at the onset of convection using scaling analysis. At the onset of convection when Ra_c= 1708 (Costa, 2002), we hypothesis that scale analysis leads to Ra of O(1000). Figure 2–10 (a) shows the situation in which Ra < Ra_c, therefore, due to the domination of diffusive transport, the fluid is quiescent and the iso-concentration lines are stratified. In Figure 2–10 (b), Ra > Ra_c. Therefore, in addition to diffusive transport with a penetration depth of δ_D, we observe fluid moving in rotating rolls with a length of Δ.
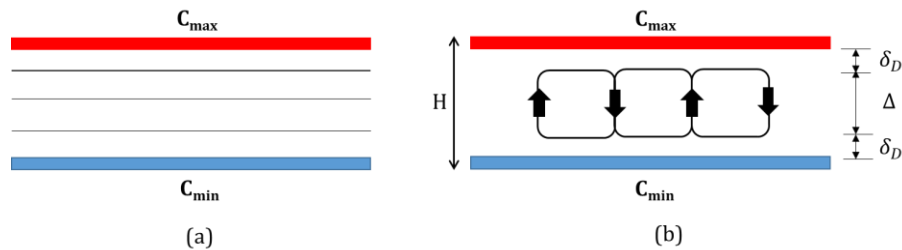
Figure 2–10: (a) Quiescent stratified fluid before the onset of convection (b) at the onset of convection.

In the absence of convective transport, the required time for molecular diffusion across the Δ layer scales as

$$(\tau_D)_\Delta \sim \frac{\Delta^2}{D} \tag{2-27}$$

In the presence of convective transport, the time scale of convective transport across the same Δ layer scales as

$$(\tau_c)_\Delta \sim \frac{\Delta}{v_c} \tag{2-28}$$

Here, v_c represents the convective velocity and scales via the momentum balance between buoyancy force ($\rho \frac{\Delta^2}{2} g\beta \frac{\Delta C}{n}$) and shear force ($2 \left(\frac{\rho v_c \nu}{\delta}\right) \frac{\Delta}{2}$) as (Bejan, 2016)

$$v_c \sim \frac{\Delta C}{n} \frac{\Delta}{H} \frac{\delta_D}{H} \frac{\rho \, g \, \beta \, H^2}{\mu} \tag{2-29}$$

Here, $\frac{\Delta C}{n}$ represents the concentration difference. Also, $\Delta = H - 2\delta_D$. By substituting Eq. (2-29) into Eq. (2-28), $(\tau_c)_\Delta$ becomes

$$(\tau_c)_\Delta \sim 2n \left(\frac{g\beta \, \Delta C \, H\rho}{\mu}\right)^{-1} \left(\frac{\delta_D}{H}\right)^{-1} \tag{2-30}$$

At the onset of convection, the convective time scale is shorter than the diffusive time scale (Costa, 2002). Therefore, at the onset of convection $\frac{(\tau_c)_\Delta}{(\tau_D)_\Delta} \sim 1$:

$$Ra_c \sim 2n \left[\frac{\delta_D}{H}\left(1 - \frac{2\delta_D}{H}\right)^2\right]^{-1} \tag{2-31}$$

Costa (2002) considered $n = 4$ and scales the concentration difference as $\frac{\Delta C}{4}$ and $\frac{\Delta C}{2}$ in the δ_D and Δ layers, respectively, which gives $\frac{\delta_D}{H} \sim \frac{\frac{\Delta C}{4}}{\Delta C} = \frac{1}{4}$. Therefore, $Ra_c \sim 128 \sim O(100)$. This is inconsistent with our first hypothesis: $Ra_c \sim O(1000)$. This error is due to the poor

definition of Δ layer (square rolls). Figure 2–8 shows that at the onset of convection, owing to the formation of primary fingers, a fraction of the Δ layer participates in convective transport. Using $\frac{\Delta}{12}$ instead of the full length of Δ (Costa, 2002), we get $Ra_c \sim 1536$ that gives $O(1000)$. Therefore, using scale analysis and physically representative scales, we are able to find $O(Ra)$ which agrees with our hypothesis.

2.4.5. Effect of Ra on CO$_2$ dissolution
2.4.5.1. CO$_2$ concentration

Figure 2–11 shows iso-concentration counters at different Ra and τ. For Ra$<10^6$, the concentration changes uniformly, suggesting that the dominant mechanism for transport is molecular diffusion. By increasing Ra, the thickness of diffusion layer (δ_D) reduces. This observation is consistent with the Einstein relationship (Einstein, 1905) in which $\delta_D \propto \sqrt{\tau}$. For Ra$=10^6$, the fingers start to emerge at $\tau=0.01$ (late times). Increasing Ra from 10^6 to 8×10^6 leads to finger formation almost 10 times earlier. Increasing Ra increases the source term ($Ra\, Sc\, C$) in Eq. (2-3) and decreases the diffusion term $\frac{1}{Ra}\left(\frac{\partial^2 C}{\partial X^2} + \frac{\partial^2 C}{\partial Y^2}\right)$ in Eq. (2-4).

For Ra$\geq10^6$, owing to the effects of effective mixing of CO$_2$ in the oil phase, the mixture is almost stagnated at the bottom of the square. Figure 2–11 confirms this observation as the streamlines near the bottom are relatively horizontal, implying that molecular diffusion is the dominant transport mechanism in this region.

Figure 2–11 shows that as Ra increases from 10^6 to 10^8, the fingers become more developed that can be explained via the definition of Ra (Squires and Quake, 2005):

$$Ra \sim \frac{(\tau_c)_\Delta}{(\tau_D)_\delta} \sim \frac{\Delta\, v_c}{D} \tag{2-32}$$

By increasing Ra from 10^6 to 10^8, Δ increases suggesting that the fingers can penetrate more deeply into the oil phase.
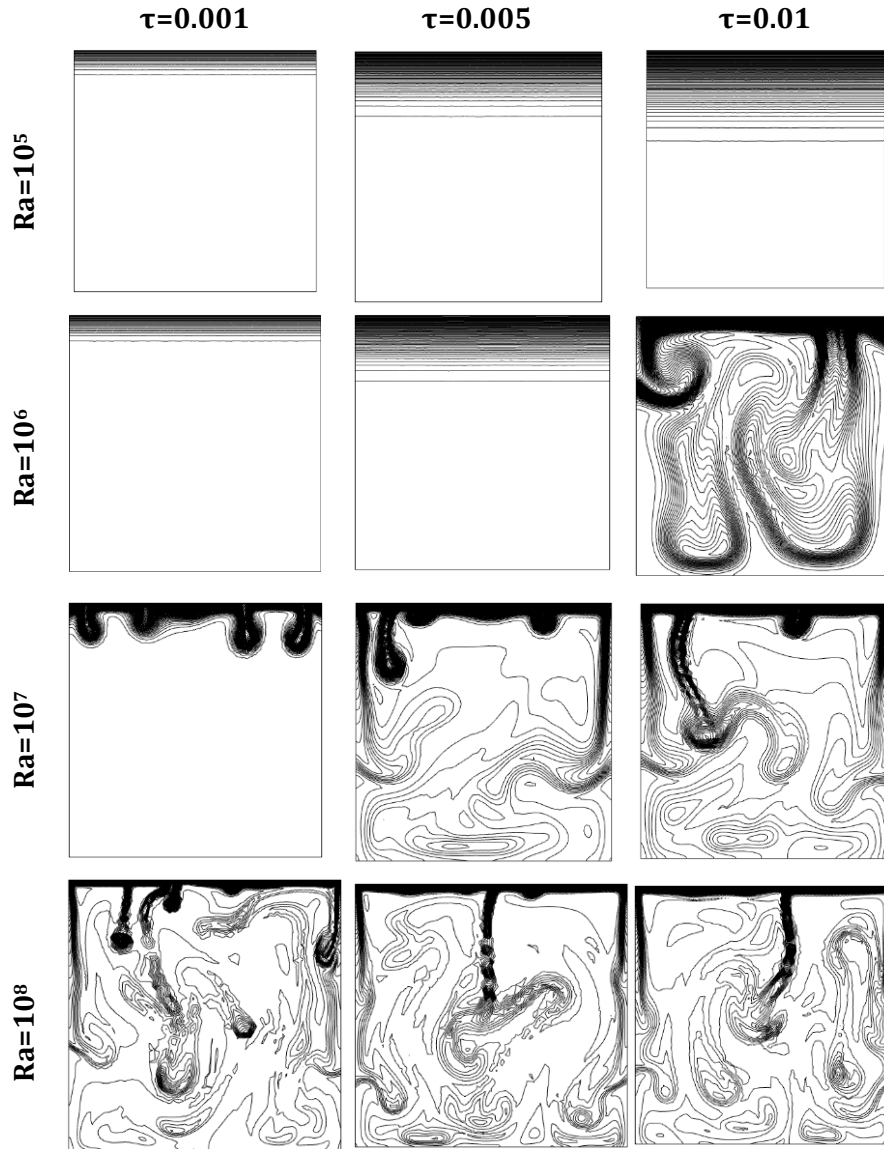
Figure 2–11: Iso-concentration contours at different values of Ra and dimensionless time. Increasing Ra leads to introducing more fingers and further development of fingers.

Figure 2–12 shows that increasing Ra leads not only to an increase in the number of fingers but also to thinner fingers. To investigate this observation, we define the wavenumber of the initial convective instabilities as $\alpha = \frac{2\pi}{\lambda}$. Here, $\lambda(m)$ represents the wavelength of the initial convective instabilities. By plotting α versus Ra in Figure 2–12, their relationship can be obtained as $\alpha = 6 \times 10^{-4}\, Ra$. Therefore, $\lambda = \frac{\pi \times 10^4}{3\, Ra}$ (Hassanzadeh et al., 2007). By

increasing Ra, the number of fingers increases (α increases) but they become thinner (λ decreases).
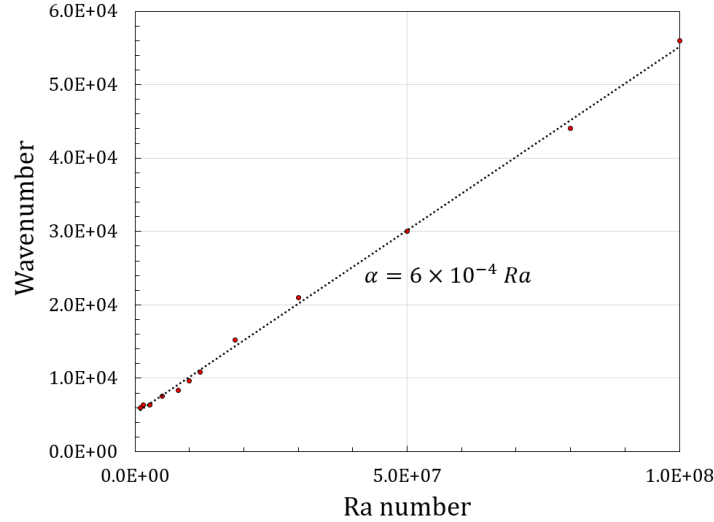
Figure 2–12: Wavenumber of initial convective instabilities versus Ra. An increasing linear trend can be observed, suggesting that increasing Ra leads to more fingers.

2.4.5.2. Concentration variance and mixing rate

Here, we study the effects of Ra as well as primary and late introduced fingers on concentration variance (σ^2) and mixing rate (ϵ). Our hypothesis is that increasing Ra increases σ^2 and decreases ϵ. We assume that primary fingers can change the trend of σ^2 and ϵ versus Ra due to producing natural convection.

Figure 2–13 (a) shows the variation of σ^2 versus dimensionless time for different values of Ra. For Ra=10^5, σ^2 increases with time. As with the case for Ra=10^5, σ^2 for Ra>10^5 also increases with time, until the first fingers produce an initial convection field in the oil phase. In fact, the existence of a convection field results in better mixing, reducing σ^2. In addition, for Ra>10^6, some fluctuations in the σ^2 curve can be observed. These fluctuations are due to the formation of small fingers. When small fingers are formed, a hump can be observed in the σ^2 curve. These new fingers are then damped, and the curve declines accordingly.

As Ra increases from 10^6 to 10^8, the rapid decline in σ^2 occurs earlier. This is due to the earlier formation of fingers at higher Ra. In addition, as Ra increases, the number of fluctuations in the σ^2 curve increases (more fingers), while the fluctuation amplitude decreases (the fingers become thinner).

For early times, a close-up view of the curve in Figure 2–13 (a) show that σ^2 reaches a maximum at Ra$=10^5$. This is due to stronger molecular diffusion at Ra$=10^5$, increasing the concentration variance.

Figure 2–13 (b) shows the variation of ϵ with τ. ϵ Rapidly decreases at earlier times for all Ra. This rapid decay corresponds to the diffusion-dominant region. For Ra$> 10^5$, after the rapid decline of ϵ, a hump can be observed, indicating the formation of initial fingers. Figure 2–13 (b) shows that increasing Ra increases the number of fluctuations and decreases the fluctuation amplitude.

(a)   (b)
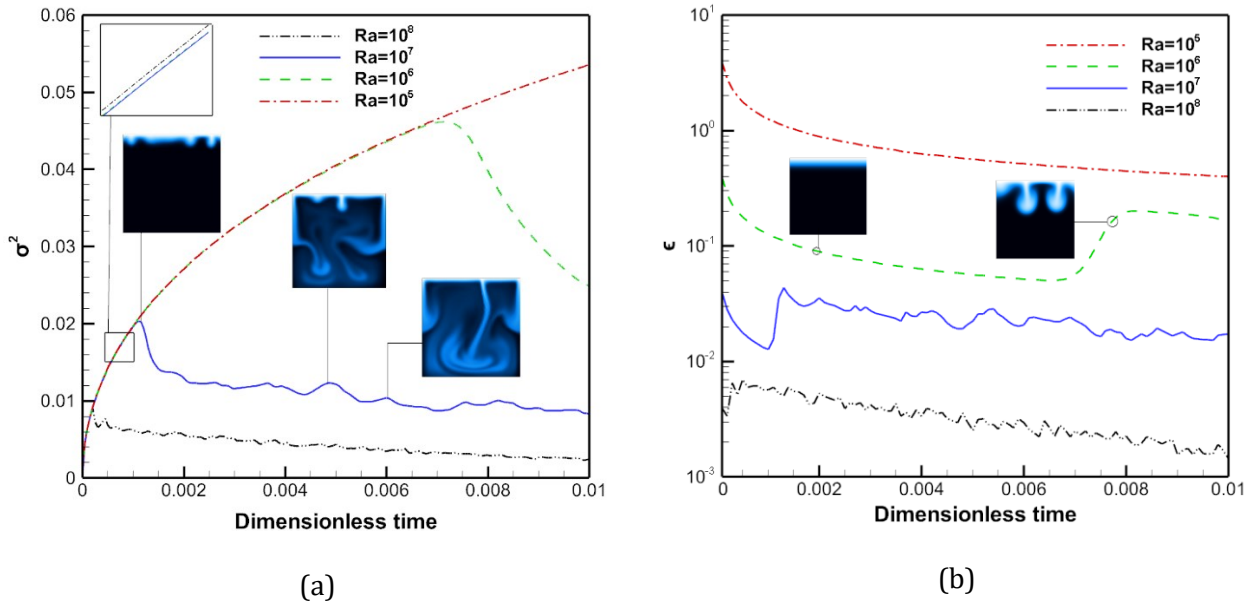
Figure 2–13: (a) Concentration variance (σ^2) versus τ for different values of Ra (b) Mixing rate (ϵ) versus τ for different values of Ra

26

2.4.5.3. Finger length

In this part, we aim to investigate the effect of Ra on finger's length. Our hypothesis is that introducing primary fingers changes the trend between Ra and fingers' length measured from the top boundary.

Figure 2–14 shows the length of the advancing fingertip versus τ in a log-log plot. For $\tau < 10^{-4}$ and all Ra values tested, a linear trend between the finger's length and time can be observed. As the molecular diffusion is the dominant transport mechanism, $\delta \propto \frac{\sqrt{D}}{H} t$. For Ra=$10^5$, this trend continues, but for Ra>10^5, a significant deviation occurs. We see that increasing Ra results in earlier deviation. In fact, this deviation is due to the formation of fingers and subsequent convective transport within the oil phase. After the deviation, a linear trend between the finger's length and time can again be observed. For Ra≥10^6, to mathematically investigate the linear trend associated with convective transport, we model each finger as a sinusoidal disturbance with wavelength λ and amplitude δ which grows exponentially (Figure 2–14).

$$\delta = \delta_0 \, e^{\beta \tau} \tag{2-33}$$

Here, β is the growth factor of the advanced finger. Calculating the slope of the straight lines associated with convective transport and comparing them with Figure 2–12, we find that $\beta \approx \alpha = 6 \times 10^{-4} \, Ra$. Therefore, Eq. (2-33) can be rewritten as

$$\delta = \delta_0 \, e^{(6 \times 10^{-4} \, Ra \, \tau)} \tag{2-34}$$
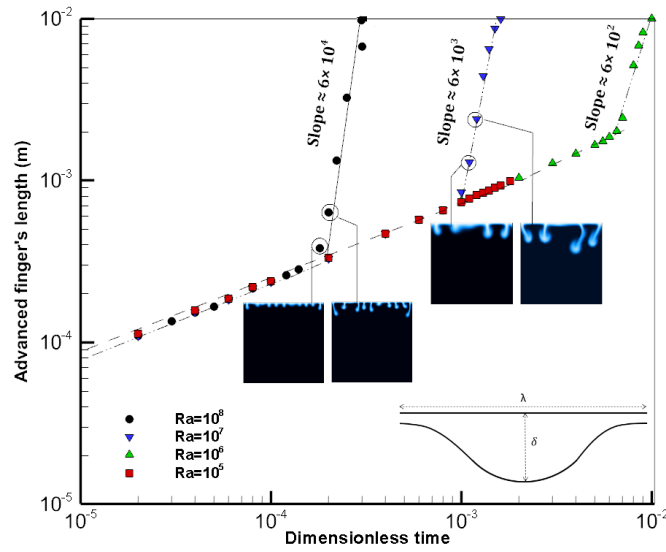
Figure 2–14: Advancing finger length versus τ for different values of Ra. Each straight line represents the dominance of one mechanism (diffusion or convection).

The required time for the concentration contour to reach to the bottom versus Ra number, is depicted in a log-log plot in Figure 2–15. This figure shows an inverse linear correlation between Ra and the required time for the advancing finger to reach the bottom. This is mainly due to more effective mixing of CO_2 in the liquid phase.
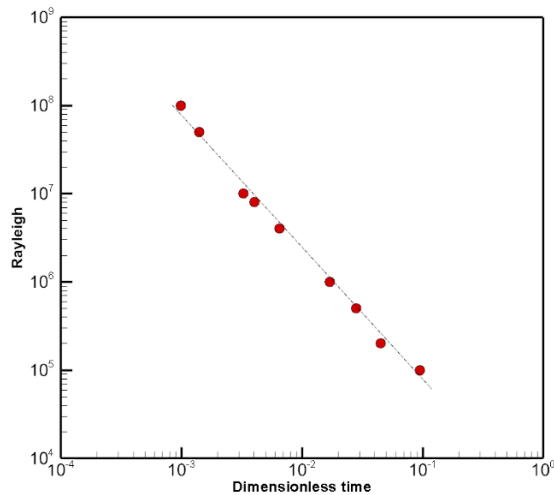
Figure 2–15: The required time for the finger's tip to reach the bottom for different Ra numbers

2.5.Summery

We have studied convective and diffusive transport and its characteristics in the CO_2 dissolution process. First, we used the turbulence analogy and interpolation-supplemented lattice Boltzmann method (ISLBM) to determine the trend between the ratio of the pseudo-diffusion coefficient to the diffusion coefficient and Rayleigh number. We then used pressure-decline data from two oil samples to investigate different periods in the CO_2 dissolution process. After that, we used an analytical approach to study the critical time and critical depth at the onset of convection. Finally, the effects of Ra on the concentration variance, mixing rate, and the finger length were investigated.

Chapter 3 : Modeling of natural-gas diffusion in oil-Saturated tight porous media

In this chapter, we provide a model for calculation the diffusion coefficient in the tight core plug. Then, we investigate the depth of gas penetration within the core. Also, the effects of adding C_2 to C_1 on the diffusion coefficient and the gas front will be studied.

3.1.Introduction

Most petroleum wells produce oil in commingle with associated gas, depending on the reservoir pressure and fluid properties. With the rapid growth in production from unconventional resources, managing excess associated gas is a challenge. It is important to note that the intensity or heat-trapping capacity of methane (the principal component of natural gas) is 25 times higher than CO_2 (Dincer and Rosen, 1999). In most cases, operators face a lack of pipeline network or it is not economically attractive to install infrastructure to effectively gather and transport these excess gas volume to the market. Natural gas emission sources include fugitive emissions, releasing gas to the atmosphere without being combusted (venting) and burning of gas at the processing facilities (flaring) (Ritchie and Roser, 2016). The loss of associated gas of any form (venting or flaring) is not only an economic issue, but also a major source of greenhouse gas emissions. According to Ritchie and Roser (2016), the natural gas emissions from oil and gas production account for 5.8% of the global greenhouse gas emissions. One way to reduce such emissions is to reinject associated gas to oil reservoirs for enhanced oil recovery.

Cyclic gas injection or huff 'n' puff (HnP) is an emerging technique that has been found as an effective way to improve oil recovery in tight reservoirs (Chen and Balhoff; Cronin et al., 2019) and reduce greenhouse gas emissions from gas flaring (Jin et al., 2017). The HnP process involves injecting gas to a targeted volume or injection pressure to a depleted oil well (huff), shutting in the well for a period of time to allow gas to permeate into the rock matrix, and finally producing back from the same well (puff or depressurization) (Carpenter, 2018). Field trials of natural-gas HnP provide a mixed picture with promising results in Eagle Ford shales (Orozco et al., 2020; Rassenfoss, 2017) and marginal

improvements in Bakken shales owing to the reservoir containment and conformance control (Kurtoglu, 2013; Rassenfoss, 2017).

Gas-transport and oil-recovery mechanisms are key factors determining the efficiency of HnP processes in tight reservoirs. The oil-recovery mechanisms involved in the process comprises oil-viscosity reduction, oil swelling, and vaporization/condensation (Alharthy et al., 2018; Baek and Akkutlu, 2019b; Carlsen et al., 2019; Zick, 1986), gas expansion (Baek and Akkutlu, 2019a; Tran et al., 2021), and pore-volume compressibility (Davudov and Moghanloo, 2019; Davudov and Moghanloo, 2018; Lan et al., 2017). Gas-transport mechanisms during injection and soaking periods of a HnP process in tight reservoirs are even more complicated and remain a subject of debate. Pressure-driven advective transport is expected to be dominant during injection and early soaking periods (Alharthy et al., 2018), while diffusive transport dominates during late times of the soaking period (Hoteit and Firoozabadi, 2006; Javadpour et al., 2007). The diffusion process in porous media is significantly hindered by the tortuous nature of the pores, cross-sectional area available for diffusion, and possibly by the pore sizes (Grathwohl, 2012). Li and Emami-Meybodi (2021) proposed a unified approach to evaluate the degree of nonlinearity of the diffusivity coefficient and transmissibility in estimating formation properties from rate transient analysis. Several studies (Carlsen et al., 2019; Cronin et al., 2019; Hoteit and Firoozabadi, 2006; Lashgari et al., 2019; Olorode et al., 2017; Yu et al., 2015) suggested that molecular diffusion is the dominant mechanism responsible for the transport of gas into the matrix during the soaking period of the HnP process in tight reservoirs.

Scaling up lab-scale gas HnP data is essential to predict field-scale response. Moghanloo et al. (2014) and Akita et al. (2018) proposed a mechanistic approach that integrates stimulated reservoir volume, pore connectivity to upscale the diffusion coefficient and oil recovery data from laboratory scale to field scale.

Several studies have reported that the phase behavior of a gas/oil system in nanopores of unconventional reservoirs deviates from the conventional ones. Teklu et al. (2016) reported that the reduction in minimum miscibility pressure (MMP) of CO_2 and CO_2/C_1 with

Bakken oil caused by confinement is pronounced when the pore size is less than 20 nm. This is caused by the critical-temperature and critical-pressure shifts. Moreover, high capillary pressure in these confined pores shrinks two-phase regions and affects equilibrium liquid/vapor-phase compositions (Nojabaei et al., 2013; Zhang et al., 2017).

There are limited experimental and analytical modeling studies to systematically investigate the diffusive-transport mechanism during the gas HnP process in tight porous media. Published studies model the process using conventional gas-transport approaches, and thus the results do not capture (i) effects of nanopore confinement on the phase behavior (Alharthy et al., 2018; Nojabaei et al., 2013; Zhang et al., 2017), (ii) fluid transport in nanometer-sized pores (Freeman et al., 2011; Perez and Devegowda, 2020), and (iii) surface chemistry during the HnP process (Baek and Akkutlu, 2019a; Bui and Akkutlu, 2017). In these works, the diffusion coefficient is estimated through the use of tortuosity models (Kerr et al., 2020). In this approach, a bulk-phase experiment should be conducted to obtain the gas -diffusion coefficient. Li et al. (2018a) investigated CO_2 diffusion process in tight rocks under elevated pressure and temperature using Schoppers' tortuosity model (Schopper, 1966). According to Lou et al. (2020), diffusion coefficients of methane in oil-saturated limestone and Bakken shale samples are in the order of 10^{-10} and 10^{-11} m^2/s, respectively. The diffusion coefficients estimated using these methods are in a wide range due to the different models presented for tortuosity factor (Moldrup et al., 2004).

According to the best authors' knowledge, there is no published work using an analytical solution to calculate the gas diffusion coefficient of the gas HnP process in tight rocks. In this chapter, we propose a novel analytical solution to quantify the diffusion coefficient, oil recovery, and pressure profile along the plug during the soaking period of the gas HnP process. First, we model the mass-transport process using pressure-declined data, mass-balance, and continuity equations. Second, the model is verified against experimental data published elsewhere (Tran et al., 2021). Next, we use the calibrated model to determine the depth of gas penetration, gas concentration, velocity, and pressure profiles along the plug.

Moreover, the effect of injection-gas enrichment (by C_2 in this study) on transport properties are also investigated.

3.2. Methodology

In this section, we first develop an analytical solution to model the gas-diffusion process during HnP process on the tight core plug. In addition, we review experimental data published in an earlier study for model validation purposes

3.2.1. Conceptual model

We design a conceptual model (Figure 3–1) to calculate the core-scale diffusion coefficient using the pressure-decline profiles. According to Figure 3–1, gas and oil transport during the HnP process occurs through the open face and other faces are considered impermeable. The model is built based on the following assumptions: (i) the soaking process is isothermal, (ii) the values of the diffusion coefficient and porosity are constant, (iii) there is no chemical reaction between gas and oil, (iv) the concentration of vaporized-oil components is negligible, (v) the changes of velocity in the r direction are negligible, and (vi) there is a first-contact miscibility process and the effects of the confinement in the nanopores are negligible.
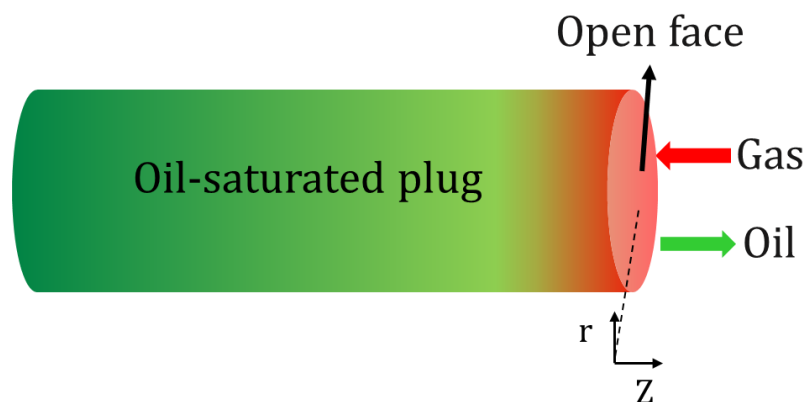
Figure 3–1: A conceptual model for modeling the gas transport. The right-hand-side face is open for gas and mass transport and other faces are sealed. It should be noted that we ignore the changes in the r direction.

3.2.2. Governing equations

For the mixture (gas + oil) shown in Figure 3-1, one can write the mass balance equation as (Bird et al., 2007; Meng et al., 2019)

$$\frac{\partial(\rho\omega_s)}{\partial t} + \frac{\partial(\rho u \omega_s)}{\partial z} = -\frac{\partial}{\partial z}\left(-\rho\frac{D}{\emptyset}\frac{\partial\omega_s}{\partial z}\right)$$

(3-1)

Where, ρ, ω_s, u, D and $\emptyset$ represent mixture's density, mass fraction of the dissolved gas into the oil, mixture's velocity, diffusion coefficient of gas in the core, and plug's porosity. The mass continuity equation for the mixture can be written as (Meng et al., 2019)

$$\frac{\partial\rho}{\partial t} = -\frac{\partial(\rho u)}{\partial z}$$

(3-2)

Based on Raoult's law, ρ can be related to ω_s as (Ott and Boerio-Goates, 2000)

$$\rho = \frac{\rho_s\rho_o}{\rho_s + \omega_s(\rho_o - \rho_s)}$$

(3-3)

It should be mentioned that in this study the gas/oil mixture is assumed to be non-volatile. This assumption is consistent with the results of our previous study (Tran et al., 2021) in which the share of vaporization in oil recovery is less than 5%.

We can write the mixture's velocity as follows (Meng et al., 2019):

$$u = \frac{(\rho_o - \rho_s)}{\rho_s + \omega_s(\rho_o - \rho_s)}\frac{D}{\emptyset}\frac{\partial\omega_s}{\partial z}$$

(3-4)

Where, ρ_o and ρ_s represent the density of oil and solvent, respectively. Details of the derivation of Eq. (3-4) are provided in Appendix A. Substituting u and ρ from Eqs. (3-3) and (3-4) into Eq. (3-1), yields (Meng et al., 2019)

$$\frac{\partial\omega_s}{\partial t} = \frac{D}{\emptyset}\left[\frac{\partial^2\omega_s}{\partial z^2} + 2\left(\frac{\partial\omega_s}{\partial z}\right)^2\frac{(\rho_s - \rho_o)}{\rho_s + \omega_s(\rho_o - \rho_s)}\right]$$

(3-5)

Eq. (3-5) can be solved to model gas transport into the system shown in Figure 3–1 with the following initial and boundary conditions:

$$\begin{cases} \omega_s\ (z,\ t=0)=0 & (3\text{-}6) \\[2mm] \omega_s\ (z=0,\ t)=\omega_{so} \\[2mm] \dfrac{\partial \omega_s\ (z\to-\infty,\ t)}{\partial z}=0 \end{cases}$$

Here, ω_{so} represents the maximum value of the solvent mass fraction in the oil measured at the average pressure during the soaking process ($\frac{P_{eq}+P_i}{2}$). The second boundary condition shows the instantons establishment of the equilibrium concentration at the core inlet. The third boundary condition implies no flow at the end of the core. The left-hand side (LHS) of Eq. (3-5) shows the accumulation of gas in the oil. The first and second terms in the right-hand sum (RHS) of Eq. (3-5) represent the changes in gas concentration due to the diffusive and convective transport, respectively (Atangana, 2018; Meng et al., 2019).

Solving Eq. (3-5) along with the initial and boundary conditions (Eq. (3-6)), yields (Meng et al., 2019)

$$\omega_s=\frac{1}{\alpha}\left(\left[1-\frac{\alpha\omega_{s0}}{1+\alpha\omega_{s0}}erfc\left(-\frac{z}{2\sqrt{\frac{D}{\emptyset}\,t}}\right)\right]^{-1}-1\right) \qquad (3\text{-}7)$$

Here, $\alpha=\frac{(\rho_o-\rho_s)}{\rho_s}$. The derivation details are presented in Appendix B. Substituting Eq. (3-7) into Eq. (3-4) gives the mixture's velocity at the core's surface ($z=0$)

$$u=\frac{\sqrt{D}\ \alpha\ \omega_{s0}}{\sqrt{\pi t\emptyset}} \qquad (3\text{-}8)$$

By Combining Eq. (3-8) and Eq. (3-2) with Darcy law, D can be calculated as

$$D = \frac{k \, \pi}{\omega_{s0}{}^2 \alpha^2 \, \mu} \frac{(p - p_{eq})}{ln \, (\frac{t_{eq}}{t})} \tag{3-9}$$

Here, p_{eq} and t_{eq} represent equilibrium pressure and the associated time for that, respectively. The detailed derivations can be found in Appendix C. We determine the value of $\frac{(p-p_{eq})}{ln \, (\frac{t_{eq}}{t})}$ using the slope of the straight line fitted to the plot of $(p - p_{eq})$ vs. $ln \, (\frac{t_{eq}}{t})$.

During the soaking period, the total produced oil's mass (m) at time t and $z=0$, can be calculated by

$$\int_0^t \emptyset \, \rho \, u \, A \, dt = m \tag{3-10}$$

Solving Eq. (3-10) using Eqs. (3-7), (3-4), and (3-3) gives

$$m = \frac{2A\sqrt{D\emptyset}\rho_o\sqrt{t}}{\sqrt{\pi}} (\frac{\omega_{s0} \, \alpha}{1 + \omega_{s0} \, \alpha}) \tag{3-11}$$

The derivation details are presented in Appendix D. Eq. (3-11) reveals that $m \propto \sqrt{t}$ and hence, $\frac{dm}{dt} \propto \frac{1}{\sqrt{t}}$.

The following integral shows the gas mole number that enters the core plug at the end of the soaking period:

$$mole = \frac{1}{M} \int_{-L}^0 \rho \, \omega_s \, A \, dz \tag{3-12}$$

Using Eq. (3-3) and (3-7), the above equation can be simplified as:

36

$$mole = \frac{A\rho_o \omega_{s0}}{M\,(1+\alpha\omega_{s0})} \int_{-L}^{0} erfc\left(\frac{-z}{2\sqrt{\frac{D}{\emptyset}t}}\right)\,dz \tag{3-13}$$

To find the distribution of ω_s along the plug we use Eq. (3-7). In addition, substituting Eq. (3-7) into Eq. (3-4) gives the distribution of u along the plug:

$$u = \frac{(\omega_{s0}\,\alpha)\,(1+\omega_s\,\alpha)\,\sqrt{D\emptyset}}{(1+\omega_{s0}\,\alpha)\,\sqrt{\pi t}}\,e^{-\frac{z^2}{4\frac{D}{\emptyset}t}} \tag{3-14}$$

3.2.3. Pressure profile along the plug

In this subsection, we develop equations to describe the pressure profile along the plug during the soaking period. We also want to investigate the effects of adding C_2 to C_1 on the pressure distribution within the plug. First, we find the equation relating pressure at the open face to the pressure inside the plug. In this regard, equating Darcy equation with Eq. (3-4) yields:

$$-\frac{k}{\mu}\frac{dp}{dz} = \frac{\alpha D}{1+\omega_s\alpha}\frac{\partial \omega_s}{\partial z} \tag{3-15}$$

Rearranging Eq. (3-15) and taking integral yields

$$-\int_{p_{z=0}}^{p_{z=-L}} dp = \int_{\omega_{s0}}^{\omega_s} \frac{\alpha\mu D}{(1+\omega_s\alpha)k}\,d\omega_s \tag{3-16}$$

The solution of Eq. (3-16) can be written as

$$p(z,t) = p(z=0,t) - \frac{\mu D}{k}\ln\left(\frac{1+\alpha\omega_s(z,t)}{1+\alpha\omega_{s0}}\right) \tag{3-17}$$

3.2.4. Experimental data

The natural-gas HnP tests on an oil-saturated ultralight core plug were conducted using a custom-designed visualization cell (Tran et al., 2021). Two sets of HnP tests were conducted with different values of initial differential pressure ($\Delta P_i = P_g - P_o$). In one test ΔP_i was set to approximately zero to model gas transport in the absence of convective gas flow. The measured pressure decline during the soaking process of the HnP tests is illustrated in

Figure 3–2. At the end of the HnP experiments, the total amount of oil produced for C_1 and C_1/C_2 tests were 0.68 g and 0.82 g, respectively.
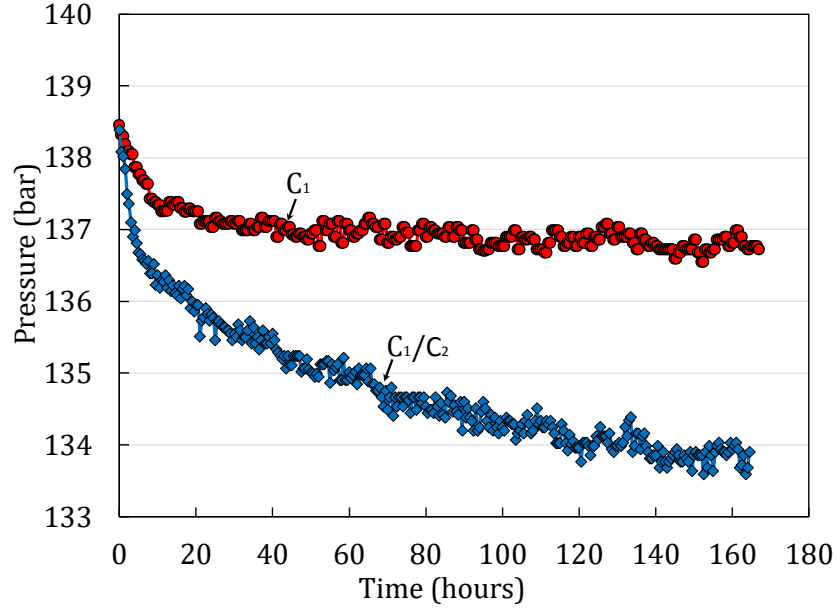
Figure 3–2: Pressure-decline profile for C_1 and C_1/C_2 during the soaking process.

3.3. Results and discussions

3.3.1. Diffusion coefficient calculation

Here, we calculate the diffusion coefficient at the core-scale using the analytical solution provided in the previous section and the pressure-decline data. Table 3–*1* lists the solvent mass fraction, oil viscosity, and the density of oil and gas for the HnP tests (Tran et al., 2021). Figure 3–3 shows the plot of $(p - p_{eq})$ vs. $ln\left(\frac{t_{eq}}{t}\right)$. From the straight lines fitted to the plots, we can determine the value of $\frac{(p - p_{eq})}{ln\left(\frac{t_{eq}}{t}\right)}$. Substituting the data listed in Table 3–1 and the slope of the fitted lines into Eq. (3-9), the diffusion coefficients for C_1 and C_1/C_2 tests can be calculated as $1.37 \times 10^{-11} \frac{m^2}{s}$ and $2.74 \times 10^{-11} \frac{m^2}{s}$, respectively. This shows that $\frac{D_{C_1/C_2}}{D_{C_1}} \approx 2$ which is consistent with the higher diffusivity of C_2 in the oil compared to C_1.

Table 3–1: Parameters used in Eq. (3-9) for calculating the diffusion coefficients.

Test	ω_{s0} (-)	μ (Pa.s)	ρ_s ($\frac{Kg}{m^3}$)	ρ_o ($\frac{Kg}{m^3}$)	α (-)
C_1	0.0334	6×10^{-3}	93.91	839	7.93
C_1/C_2	0.0665	6×10^{-3}	132.12	839	5.35
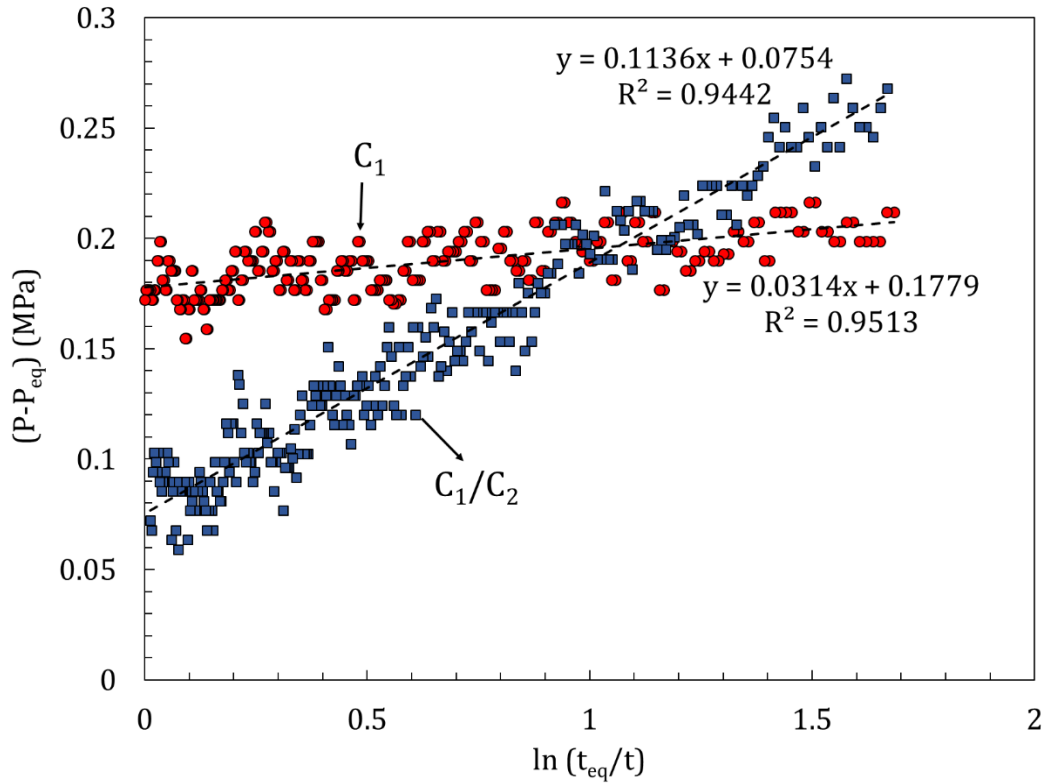
Figure 3–3: A plot of $(p - p_{eq})$ vs. $ln\ (\frac{t_{eq}}{t})$. Higher slope for the C_1/C_2 curve can be observed, suggesting higher solubility of C_2 in the oil.

Table 3–2 presents the estimated D values using Eq. (3-9) and those reported in the literature. As can be seen, a discrepancy of one order of magnitude in D values is observed in previous studies, which consider either different tortuosity models or numerical methods. On the other hand, the D values obtained in this study can be validated through thermodynamic analysis and will be discussed in a later section.

Table 3–2: Comparison of the D calculated in this study with the values reported in the literature.

Rock Sample	Porosity (% bulk volume)	Fluid System	Pressure (bar) and Temperature (°C)	D (m²/s)	Reference
Montney siltstone	3.5	C_1/Montney oil	137.9 and 50	1.37×10^{-11}	This work
Montney siltstone	3.5	C_1/C_2:70/30 mol% and Montney oil	137.9 and 50	2.74×10^{-11}	This work
Montney siltstone	3.5	C_1/Montney oil	137.9 and 50	1.75×10^{-10}	Tortuosity model by Tran et al. (2021)
Montney siltstone	3.5	C_1/C_2:70/30 mol% and Montney oil	137.9 and 50	2.28×10^{-10}	Tortuosity model by Tran et al. (2021)
Indiana limestone	15-18	C_1/Bakken oil	137.9 and 21	1.50×10^{-10}	Tortuosity model by Lou et al. (2019)
Bakken shale	8	C_1/Bakken oil	137.9 and 21	2.00×10^{-11}	Tortuosity model by Lou et al. (2020)
Marine shales	-	C_1/C_2:72/28 mol% and black oil	303 and 82	4.50×10^{-10}	Molecular dynamic simulation by Perez and Devegowda (2020)

Also, we wish to find the value of tortuosity for our study by comparing the calculated value of diffusion coefficient in the core scale (D) with that of bulk phase (D_0). Lou et al. (2019) suggested the following equation for tortuosity (τ) calculation in the Bakken shale:

$$\tau = \frac{D_0 \emptyset}{D} D \qquad (3\text{-}18)$$

They reported $\tau = 12.8$ as the tortuosity value for the Bakken shale (Lou et al., 2019)Regarding the value of τ for the current study, Tran et al. (2021) calculated bulk phase diffusion

coefficients' value of C_1 and C_1/C_2 as 5×10^{-9} and $6.5 \times 10^{-9} \frac{m^2}{s}$, respectively. Therefore, using Eq. (3-18), the tortuosity for our study can be calculated as $\frac{D_{C_1}\emptyset}{D_{0C_1}} = 12.77$, which is in the good agreement with the reported results in the literature (Lou et al., 2019).

3.3.2. Oil production during soaking period

In this subsection, we calculate the oil production during soaking period using our analytical model. Using the experimental data, we are able to decouple the amount of produced oil during soaking and depressurization periods and determine their relative contribution to the total oil recovery. We also evaluate the effects of enriching injection gas by C_2 on oil production using Eq. (3-11) and diffusion coefficient.

To plot the produced oil mass (m) versus time for C_1 and C_1/C_2, we substitute the obtained values for D into Eq. (11). Figure 3–4 (a) and (b) show the oil rate and cumulative oil production, respectively. It can be seen that, the oil rate production $\propto \frac{1}{\sqrt{t}}$ and cumulative oil production $\propto \sqrt{t}$. Comparing Figure 3–4 (a) and Figure 3–2 reveals that the maximum oil rate production is associated with the maximum pressure drop which occurs at $t < 10$ hrs. In addition, increasing the pressure-decline slope improves the oil production rate. Adding C_2 to C_1 results in higher oil rate production and increases the ultimate oil recovery by 46%.

Table 3–3 lists the calculated and measured values of the produced oil at the end of the soaking and depressurization periods, respectively. During the soaking period, adding 30 mol% C_2 to the injection gas increases oil recovery by 3%. In addition, the oil recovery during the soaking period is less than 20% of the total recovery.

(a)   (b)
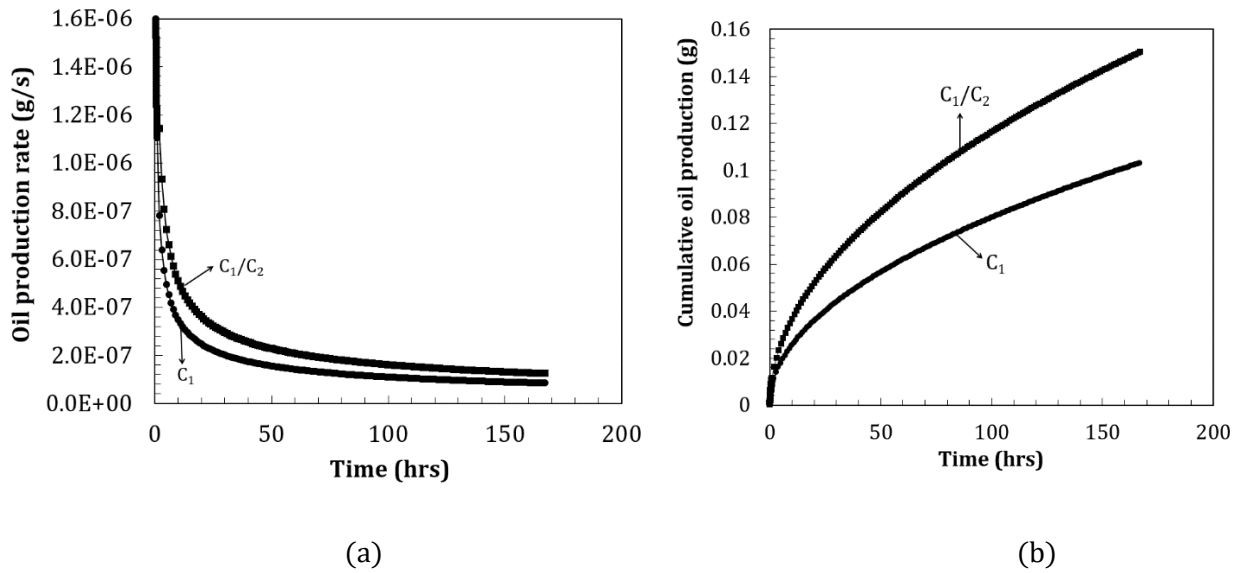
Figure 3–4: (a) Oil production rate and (b) cumulative oil production versus time for C_1 and C_1/C_2. Adding C_2 to the C_1 increases the oil production rate.

Table 3–3: Oil recovery by the end of the soaking and puff processes. The share of the soaking period in the total oil recovery is less than 20%.

Test	Calculated Oil recovery at the end of soaking (g)	Total oil recovery (measured) (g)	Share of the soaking in the total oil recovery
C_1	0.1029	0.6895	14%
C_1/C_2	0.1504	0.8376	17%

3.3.3. Distribution of ω_s and u within the core plug

We present the results of gas penetration depth and the distribution of the mixture's velocity in the plug for both C_1 and C_1/C_2 tests. The impacts of adding C_2 to C_1 on the penetration depth and the mixture's velocity are investigated.

Figure 3–5 (a) and (b) show the distribution of ω_s along the core plug for C_1 and C_1/C_2 tests, respectively. For the C_1 test, the ultimate gas penetration depth is around 4.2 cm (65% of the core's length). By adding C_2 to C_1, the gas can reach the end of the core. Also, $\frac{d\omega_s}{dt}\big|_{C1/C2} > \frac{d\omega_s}{dt}\big|_{C1}$ which reveals more gas accumulation during C_1/C_2 test. This observation is consistent with $\frac{D_{C1/C2}}{D_{C1}} \approx 2$, obtained in the previous part. For both tests, $\frac{d\omega_s}{dz}$ and $\frac{dp}{dt}$ decrease by increasing time. In fact, decreasing the concentration gradient decreases the pressure drop.

Figure 3–5 (b) and (c) represent the plot of u versus distance from the open face for C_1 and C_1/C_2 tests, respectively. $u\big|_{C1/C2} > u\big|_{C1}$, suggesting higher solubility and more oil swelling by adding C_2 to C_1. At early times, we observe a sharp decline in u curves associated with the steep decrease in the ω_s. As $u \propto \frac{dp}{dz} \propto (\frac{dp}{dt})^{\frac{1}{2}}$ (see Eq. (D-4)), a sharp decline at early times can be observed. By increasing the time, the velocity curves tend to become linear, suggesting a more uniform distribution of ω_s. By increasing the time, $\frac{du}{dt}$ (acceleration term) decreases, indicating a lower oil production rate. Comparing ω_s and u curves shows that u decreases as ω_s and subsequently concentration gradient reduces (e.g. $u = 0$ @ $\omega_s = 0$). This observation endorses the role of molecular diffusion as the dominant mechanism during the soaking period.

(a)

(b)

(c)   (d)
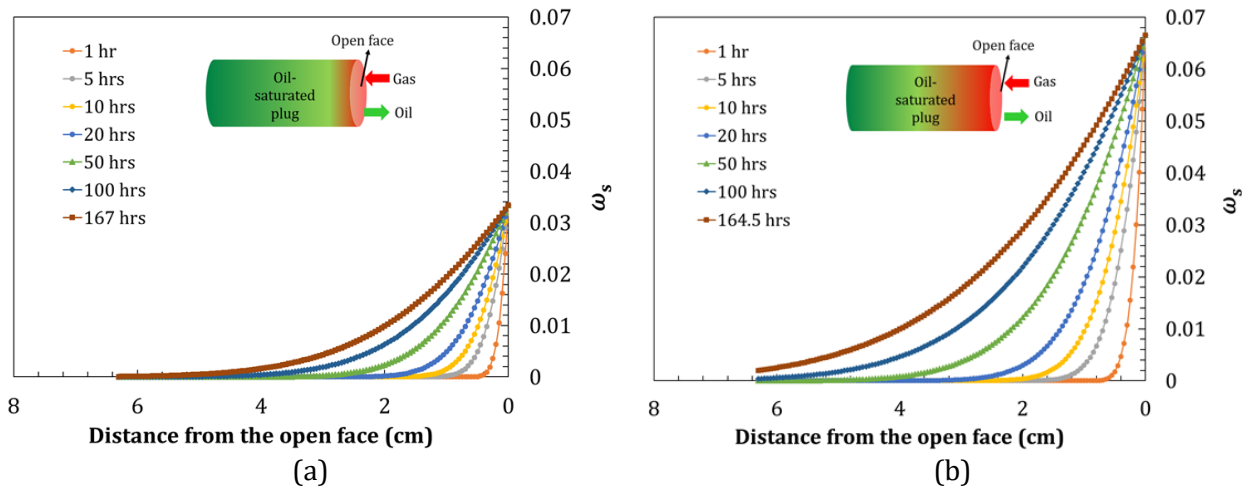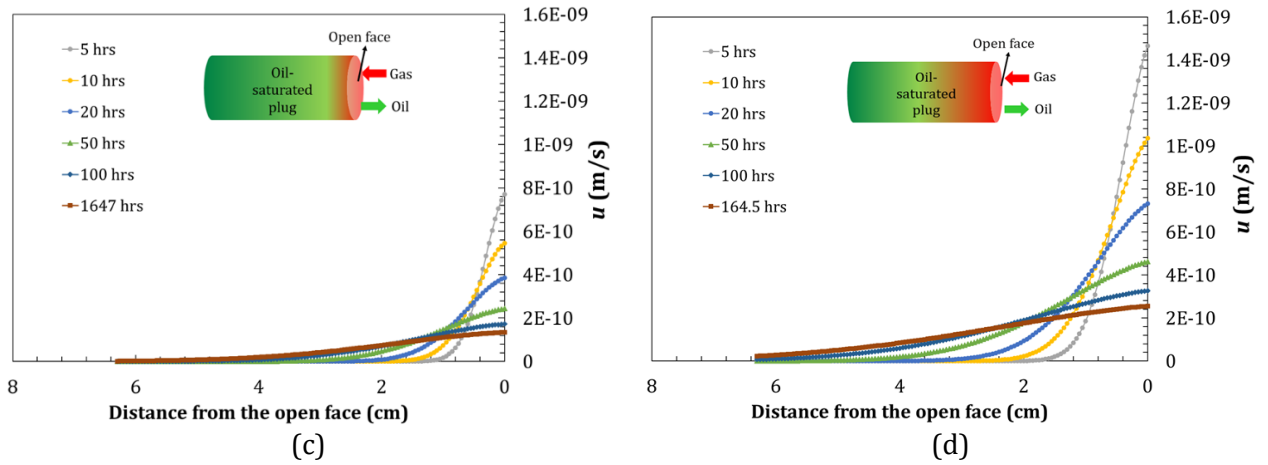
Figure 3–5: Distribution of ω_s along the core plug for (a) C_1 and (b) C_1/C_2 tests. Distribution of u along the core plug for the (c) C_1 and (d) C_1/C_2 tests.

3.3.4. Pressure distribution along the core plug

Figure 3–6 (a) and (b) represent the pressure distribution along the core plug for C_1 and C_1/C_2 tests, respectively. We observe that the pressure within the core increasing by increasing the distance from the core face. On the other hand, the reason for gas penetration into the core is the gradient in the gas concentration. Comparing Figure 3–6 (a) and (b) reveals that adding C_2 to C_1 results in higher pressure within the core (~0.5 MPa). This observation is consistent with higher oil production for C_2/C_1 test (Table 3). Higher pressure within the core yields more oil recovery. Also, the presence of C_2 in injection gas leads to a faster pressure decline owing to a higher diffusion coefficient ($\frac{D_{C1/C2}}{D_{C1}} \approx 2$) and mass transfer rate.
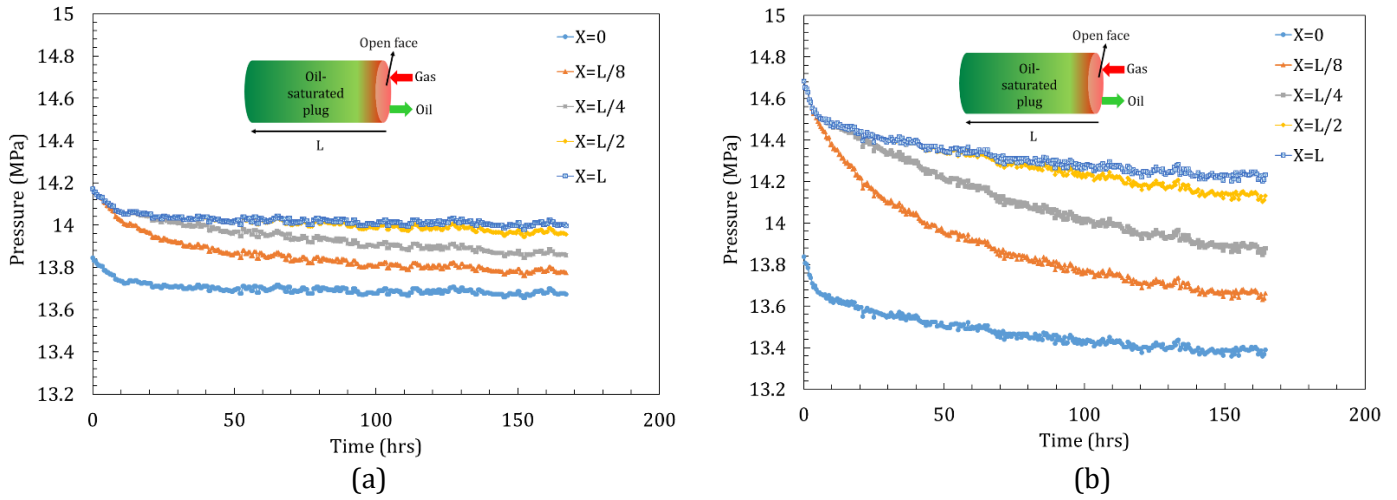
Figure 3–6: Pressure-decline curves versus time at different points within the core plug for (a) C_1 and (b) C_1/C_2 tests.

3.3.5. Thermodynamic consistency checks

Since the analytical model is calibrated against the measured pressure-decline and oil production data, consistency checks should be made to ensure the validity of the calculated diffusion coefficient, gas-penetration depth, and pressure profile. Table 3–*4* lists the pressure, volume, density, and the number of moles before and after the soaking period for each test (Tran et al., 2021). The gas density at each pressure is calculated using the Peng-Robinson equation of state.

Table 3–4: Thermodynamic properties of C1 and C1/C2 tests during the soaking period (Tran et al., 2021)

Test	Before the soaking period				After the soaking period				$\Delta n = n_2 - n_1$ (mole)
	P (bar)	V (cc)	ρ (gr/cc)	n_1 (mole)	P (bar)	V (cc)	ρ (gr/cc)	n_2 (mole)	
C_1	138.44	326	0.09	1.92	136.65	326	0.09	1.89	0.024
C_1/C_2	138.37	326	0.14	2.19	133.62	326	0.13	2.11	0.081

Using the calculated diffusion coefficients and the data provided in Table 3–2, Eq. (3-13) can be solved analytically. Therefore, the number of moles of leaked-off gas for C_1 and C_1/C_2 are 0.024 and 0.080, respectively. Comparing the obtained values from Eq. (3-13) with experimental values in Table 3–4 ($\Delta n = 0.026, 0.081$), the average relative deviation (AARD) for the calculated moles of leaked-off gas is 4%.

3.3.6. Effect of dispersion on diffusion coefficient calculation

In this subsection, we wish to investigate the effect of dispersion on the calculated values of diffusion coefficient in the core-scale. To this end, we can consider the following equation which counts the effect of dispersion (Fried and Combarnous, 1971):

$$K = D + \alpha\left(\frac{a^2 u^2}{D_0}\right)$$ (3-19)

Where, D, K, a and D_0 are diffusion coefficient in the core scale, effective diffusion, characteristic dimension of the cross section and the diffusion coefficient in the bulk phase, respectively. In fact, term $\alpha\left(\frac{a^2 u^2}{D_0}\right)$ in the above equation shows the effect of dispersion. Fried and Combarnous (1971) considered $\alpha < 1$ and $a = \frac{1}{48}$. Also, $u \sim O$ (10^{-10}) and $D_0 \sim O$ (10^{-9}) for both C_1 and C_1/C_2 tests (Tran et al., 2021). Therefore, $\alpha\left(\frac{a^2 u^2}{D_0}\right)$ is expected to be from O (10^{-14}). By comparing $D \sim O$ (10^{-11}) and $\alpha\left(\frac{a^2 u^2}{D_0}\right) \sim O$ (10^{-14}), we conclude that the effect of dispersion in our study is negligible.

3.4. Summery

In this chapter, we proposed an analytical solution capable of modeling the gas-diffusion process, and estimating the diffusion coefficient and depth of gas penetration during the soaking period of a cyclic gas injection process in tight porous media. We also investigate the effects of adding C_2 to C_1 on the diffusion coefficient, gas penetration depth and the pressure distribution along the core. This analytical solution is a useful method for estimating the diffusion coefficient and depth of gas penetration during the soaking period of a cyclic gas injection process from experimental or field data.

Chapter 4 : Conclusions and future work

4.1.Conclusions

This study entails two main parts (i) numerical and analytical study of CO_2 dissolution in the condensate and crude oils (ii) calculation diffusion coefficient in the pore-scale.

In the first part, we used turbulence analogy and Interpolation Supplementary Lattice Boltzmann Method to find the effects of convection field as well as density driven fingers on the diffusive and convective transports. From this part, the following concluding remarks are obtained:

- The ratio of the pseudo-diffusion coefficient to the diffusion coefficient ($\frac{D^*}{D}$) increases with Ra logarithmically.

- During the CO_2 dissolution process in condensate and crude oils, three distinct periods can be identified, corresponding to (i) diffusive transport (ii) early convection and (iii) late convection.

- The early convective period is responsible for more than 50% of ultimate CO_2 dissolution for both condensate and crude oils.

- The critical time at the onset of convection depends on the diffusion coefficient, viscosity and the change in density due to CO_2 dissolution.

- Scale analysis shows that at the onset of convection, Ra ~ O(1000) which is consistent with the accepted value for the onset of Rayleigh-Benard convection (Ra=1708).

- The wavenumber of initial convective instabilities increases linearly with increasing Ra, suggesting that by increasing Ra the number of fingers increases.

- The wavenumber of initial convective instabilities is almost equal to the growth factor of the advanced finger.

In the second part, we presented a novel method to calculate the diffusion coefficient in the tight core plug during the soaking process. We were able to find the relationship between the produced oil and time during the soaking period. Also, the distribution of pressure and the gas front within the core were investigated. Our main conclusions are the followings:

- The diffusion coefficient and velocity are controlled by pressure gradient at the early soaking times and concentration gradient when the soaking progresses.

- The use of gas mixtures increases the gas difussion rate, owing to the higher solubility of C_2 in oil compared to C_1.

- The depth of gas penetration in the plug is strongly dependent on the composition of injection gas. We found that the gas front reaches the other end of the plug in the gas-mixture case after a 7-day soaking period.

- The proposed model can be used to predict the expanded oil volume by gas dissolution during the soaking period. The estimated values are in the range of experimental results.

- The pressure gradient in the core is driven by advective transport at the early times, while its direction is reverse due to oil swelling, leading to counter-current oil production.

4.2.Future work

Modeling puff period and finding the relationship between the produced oil and time is recommended. Also, the researchers can find the optimum pressure drop during the puff period by proper modeling of depressurization. In this regard, modeling of two phase flow (oil and gas) in the porous media is needed.

In the current work work, assumed that the diffusion coefficient is constant during the soaking period. However, diffusion coefficient can be considered as a function of the gas concentration in the core plug. Finding an analytical solution for the diffusion coefficient in the pore-scale when it depends on the gas saturation, is interesting.

Bibliography

Ahangar, E.K., Fallah-Kharmiani, S., Khakhian, S.D., Lian-PingWang, 2020. A lattice Boltzmann study of rarefied gaseous flow with convective heat transfer in backward facing micro-step. Physics of Fluids 32(6), 062005.

Akita, E., Moghanloo, R.G., Davudov, D., Tinni, A., 2018. A Systematic Approach for Upscaling of the EOR Results from Lab-Scale to Well-Scale in Liquid-Rich Shale Plays, SPE Improved Oil Recovery Conference. Society of Petroleum Engineers.

Alharthy, N., Teklu, T., Kazemi, H., Graves, R., Hawthorne, S., Braunberger, J., Kurtoglu, B.J.S.R.E., Engineering, 2018. Enhanced Oil Recovery in Liquid–Rich Shale Reservoirs: Laboratory to Field. 21(01), 137-159.

Ashcroft, S.J., Isa, M.B., 1997. Effect of dissolved gases on the densities of hydrocarbons. Journal of Chemical & Engineering Data 42(6), 1244-1248.

Atangana, A., 2018. Chapter 3 - Groundwater Pollution, in: Atangana, A. (Ed.) Fractional Operators with Constant and Variable Order with Application to Geo-Hydrology. Academic Press, pp. 49-72.

Baek, S., Akkutlu, I.Y.J.S.J., 2019a. Mean Free Path of Gas Molecules in Organic Nanochannels Using Molecular Simulations. 24(06), 2,555-552,573.

Baek, S., Akkutlu, I.Y.J.S.J., 2019b. Produced-fluid composition redistribution in source rocks for hydrocarbon-in-place and thermodynamic recovery calculations. 24(03), 1,395-391,414.

Bejan, A., 2016. Advanced engineering thermodynamics. John Wiley & Sons. Berkhin, P., 2006. A survey of clustering data mining techniques, Grouping multidimensional data. Springer, pp. 25-71.

Bird, R., Stewart, W., Lightfoot, E., 2007. Mass transport. [1]ransport Phenomena. Basel: John Wiley and Sons, 495.

Briefing, U.S.J.U.E.I.A., 2020. International energy outlook 2020.

Bui, K., Akkutlu, I.Y.J.S.J., 2017. Hydrocarbons recovery from model-kerogen nanopores. 22(03), 854-862.

Carlsen, M., Whitson*, C., Dahouk, M.M., Younus, B., Yusra, I., Kerr, E., Nohavitza, J., Thuesen, M., Drozd, J., Ambrose, R., 2019. Compositional tracking of a Huff-n-Puff project in the eagle ford, Unconventional Resources Technology Conference, Denver, Colorado, 22-24 July 2019. Unconventional Resources Technology Conference (URTeC); Society of Petroleum Engineering, pp. 4675-4699.

Carpenter, C., 2018. A Review of Improved-Oil-Recovery Methods in North American Unconventional Reservoirs. Journal of Petroleum Technology 70(01), 42-44.

Carpenter, C.J.J.o.P.T., 2018. Huff'n'Puff Gas-Injection Pilot Improves Oil Recovery in the Eagle Ford. 70(11), 91-92.

Chen, C., Balhoff, M.J.S.o.P.E.d., &Mohanty KK (2014). Effect of Reservoir Heterogeneity on Primary Recovery and CO2 Huff" n" Puff Recovery in Shale-Oil Reservoirs. 10.

Costa, V., 2002. A time scale-based analysis of the laminar convective phenomena. International journal of thermal sciences 41(12), 1131-1140.

Cronin, M., Emami-Meybodi, H., Johns, R.T.J.S.J., 2019. Diffusion-dominated proxy model for solvent injection in ultratight oil reservoirs. 24(02), 660-680.

Csanady, G.T., 2012. Turbulent diffusion in the environment. Springer Science & Business Media.

Cui, L., Ma, K., Puerto, M., Abdala, A.A., Tanakov, I., Lu, L.J., Chen, Y., Elhag, A., Johnston, K.P., Biswal, S.L.J.S.J., 2016. Mobility of ethomeen C12 and carbon dioxide (CO2) foam at high temperature/high salinity and in carbonate cores. 21(04), 1151-1163.

Damen, K., Faaij, A., van Bergen, F., Gale, J., Lysen, E., 2005. Identification of early opportunities for CO2 sequestration—worldwide screening for CO2-EOR and CO2-ECBM projects. Energy 30(10), 1931-1952.

Davudov, D., Moghanloo, R.G.J.F., 2019. A new model for permeability impairment due to asphaltene deposition. 235, 239-248.

Davudov, D., Moghanloo, R.G.J.I.J.o.C.G., 2018. Impact of pore compressibility and connectivity loss on shale permeability. 187, 98-113.

Dincer, I., Rosen, M.A.J.A.e., 1999. Energy, environment and sustainable development. 64(1-4), 427-440.

Dixit, H.N., Babu, V., 2006. Simulation of high Rayleigh number natural convection in a square cavity using the lattice Boltzmann method. International Journal of Heat and Mass Transfer 49(3), 727-739.

Drazin, P.G., 2002. Introduction to hydrodynamic stability. Cambridge university press.

Einstein, A., 1905. Über die von der molekularkinetischen Theorie der Wärme geforderte Bewegung von in ruhenden Flüssigkeiten suspendierten Teilchen. Annalen der physik 322(8), 549-560.

Farajzadeh, R., Barati, A., Delil, H.A., Bruining, J., Zitha, P.L., 2007. Mass transfer of CO2 into water and surfactant solutions. Petroleum Science and Technology 25(12), 1493-1511.

Fattahi, A., Hosseinalipour, S.M., Karimi, N., 2017. On the dissipation and dispersion of entropy waves in heat transferring channel flows. Physics of Fluids 29(8), 087104.

Freeman, C., Moridis, G., Blasingame, T.J.T.i.p.m., 2011. A numerical study of microscale flow behavior in tight gas and shale gas reservoir systems. 90(1), 253-268.

Fried, J. J., and M. A. Combarnous. "Dispersion in porous media." In *Advances in hydroscience*, vol. 7, pp. 169-282. Elsevier, 1971.

Ghanbarnezhad Moghanloo, R., Hosseinipoor, S., 2014. The Mechanistic Modeling of Fluid Flow in Shale, Unconventional Resources Technology Conference, Denver, Colorado, 25-27 August 2014. Society of Exploration Geophysicists, American Association of Petroleum ..., pp. 2281-2305.

Ghasemi, K., Siavashi, M., 2017. Lattice Boltzmann numerical simulation and entropy generation analysis of natural convection of nanofluid in a porous cavity with different linear temperature distributions on side walls. Journal of Molecular Liquids 233, 415-430.

Ghorbani, Z., Riaz, A., Daniel, D., 2017. Convective mixing in vertically-layered porous media: The linear regime and the onset of convection. Physics of Fluids 29(8), 084101.

Grathwohl, P., 2012. Diffusion in natural porous media: contaminant transport, sorption/desorption and dissolution kinetics. Springer Science & Business Media.

Guerrero-Martínez, F.J., Younger, P.L., Karimi, N., Kyriakis, S., 2017. Three-dimensional numerical simulations of free convection in a layered porous enclosure. International Journal of Heat and Mass Transfer 106, 1005-1013.

Guo, P., Wang, Z., Shen, P., Du, J.J.I., research, e.c., 2009. Molecular diffusion coefficients of the multicomponent gas— crude oil systems under high temperature and pressure. 48(19), 9023-9027.

Guo, Z., Shu, C., 2013. Lattice Boltzmann method and its applications in engineering. World Scientific.

Haas, A., Gmelin, L., Meyer, R.J., Pietsch, E., Fluck, E., 1973. Gmelins Handbuch der anorganischen Chemie. 8. Aufl. Ergänzungswerk. Bd. 9: Perfluorhalogenorgano-Verbindungen der Hauptgruppenelemente. Tl. 1: Verbindungen von Schwefel: Perfluorhalogenorgano-Verbindungen der Hauptgruppenelemente 1. Verlag Chemie.

Hassanzadeh, H., 2006. Mathematical modeling of convective mixing in porous media for geological CO2 storage.

Hassanzadeh, H., Pooladi-Darvish, M., Keith, D., 2005. Modelling of convective mixing in co storage. Journal of Canadian Petroleum Technology 44(10).

Hassanzadeh, H., Pooladi-Darvish, M., Keith, D.W., 2007. Scaling behavior of convective mixing, with application to geological storage of CO2. AIChE journal 53(5), 1121-1131.

Hoteit, H., Firoozabadi, A., 2006. Numerical modeling of diffusion in fractured media for gas injection and recycling schemes, SPE Annual Technical Conference and Exhibition. Society of Petroleum Engineers.

Huang, K., Zhu, W., Sun, L., Wang, Q., Liu, Q., 2019. Experimental study on gas EOR for heavy oil in glutenite reservoirs after water flooding. Journal of Petroleum Science and Engineering 181, 106130.

Hughes, J.D., 2013. A reality check on the shale revolution. Nature 494(7437), 307-308.

Izadi, A., Siavashi, M., Rasam, H., Xiong, Q., 2020. MHD enhanced nanofluid mediated heat transfer in porous metal for CPU cooling. Applied Thermal Engineering 168, 114843.

James, L.A., Ioannidis, M.A., Chatzis, I., 2012. Experimentally validated model for the determination of concentration-dependent diffusion of a light hydrocarbon in bitumen. Energy & fuels 26(10), 6200-6209.

Jami, M., Moufekkir, F., Mezrhab, A., Fontaine, J.P., Bouzidi, M.h., 2016. New thermal MRT lattice Boltzmann method for simulations of convective flows. International Journal of Thermal Sciences 100, 98-107.

Janiga, D., Czarnota, R., Kuk, E., Stopa, J., Wojnarowski, P.J.J.o.P.S., Engineering, 2020. Measurement of Oil-CO2 diffusion coefficient using pulse-echo method for pressure-volume decay approach under reservoir conditions. 185, 106636.

Javadpour, F., Fisher, D., Unsworth, M.J.J.o.C.P.T., 2007. Nanoscale gas flow in shale gas sediments. 46(10).

Jha, B., Cueto-Felgueroso, L., Juanes, R., 2011. Fluid Mixing from Viscous Fingering. Physical Review Letters 106(19), 194502.

Jin, L., Hawthorne, S., Sorensen, J., Pekot, L., Bosshart, N., Gorecki, C., Steadman, E., Harju, J., 2017. Utilization of produced gas for improved oil recovery

and reduced emissions from the Bakken formation, SPE Health, Safety, Security, Environment, & Social Responsibility Conference-North America. Society of Petroleum Engineers.

Kalteh, M., Hasani, H., 2014. Lattice Boltzmann simulation of nanofluid free convection heat transfer in an L-shaped enclosure. Superlattices and Microstructures 66, 112-128.

Karimi, N., McGrath, S., Brown, P., Weinkauff, J., Dreizler, A., 2016. Generation of adverse pressure gradient in the circumferential flashback of a premixed flame. Flow, Turbulence and Combustion 97(2), 663-687.

Kefayati, G., 2020. An immersed boundary-lattice Boltzmann method for thermal and thermo-solutal problems of Newtonian and non-Newtonian fluids. Physics of Fluids 32(7), 073103.

Kerr, E., Venepalli, K.K., Patel, K., Ambrose, R., Erdle, J., 2020. Use of reservoir simulation to forecast field EOR response-An eagle ford gas injection Huff-N-Puff application, SPE Hydraulic Fracturing Technology Conference and Exhibition. Society of Petroleum Engineers.

Khosrokhavar, R., 2015. Mechanisms for CO2 Sequestration in Geological Formations and Enhanced Gas Recovery. Springer.

Kumar, S., Mandal, A., 2017. A comprehensive review on chemically enhanced water alternating gas/CO2 (CEWAG) injection for enhanced oil recovery. Journal of Petroleum Science and Engineering 157, 696-715.

Kurtoglu, B., 2013. Integrated reservoir characterization and modeling in support of enhanced oil recovery for Bakken. Colorado School of Mines.

Kuznik, F., Vareilles, J., Rusaouen, G., Krauss, G., 2007. A double-population lattice Boltzmann method with non-uniform mesh for the simulation of natural convection in a square cavity. International Journal of Heat and Fluid Flow 28(5), 862-870.

Lan, Y., Moghanloo, R.G., Davudov, D.J.S.J., 2017. Pore compressibility of shale formations. 22(06), 1,778-771,789.

Lashgari, H.R., Sun, A., Zhang, T., Pope, G.A., Lake, L.W.J.F., 2019. Evaluation of carbon dioxide storage and miscible gas EOR in shale oil reservoirs. 241, 1223-1235.

Li, H.A., Sun, H., Yang, D.J.H., Transfer, M., 2017. Effective diffusion coefficients of gas mixture in heavy oil under constant-pressure conditions. 53(5), 1527-1540.

Li, S., Qiao, C., Zhang, C., Li, Z., 2018a. Determination of diffusion coefficients of supercritical CO_2 under tight oil reservoir conditions with pressure-decay method. Journal of CO_2 Utilization 24, 430-443.

Li, S., Qiao, C., Zhang, C., Li, Z.J.J.o.C.U., 2018b. Determination of diffusion coefficients of supercritical CO_2 under tight oil reservoir conditions with pressure-decay method. 24, 430-443.

Lindeberg, E., Bergmo, P., 2003. The long-term fate of CO_2 injected into an aquifer. Greenhouse gas control technologies 1, 489-494.

Lindeberg, E., Wessel-Berg, D., 1997. Vertical convection in an aquifer column under a gas cap of CO_2. Energy Conversion and management 38, S229-S234.

Liu, Z., Emami-Meybodi, H.J.S.J., 2021. A Unified Approach to the Nonlinearity of the Diffusivity Equation and Assessment of Pseudotime. 26(01), 241-261.

Lou, X., Chakraborty, N., Karpyn, Z., Ayala, L., Nagarajan, N., Wijaya, Z., 2019. Experimental study of gas-liquid diffusion in porous rocks and bulk fluids to investigate the effect of rock matrix hindrance, SPE Annual Technical Conference and Exhibition. Society of Petroleum Engineers.

Lou, X., Chakraborty, N., Karpyn, Z.T., Ayala, L.F., Nagarajan, N., Wijaya, Z., 2020. Experimental Study of Gas/Liquid Diffusion in Porous Rocks and Bulk Fluids to Investigate the Effect of Rock-Matrix Hindrance. SPE-50941-PA.

Lu, C., Lichtner, P.C., 2007. High resolution numerical investigation on the effect of convective instability on long term CO_2 storage in saline aquifers, Journal of Physics: Conference Series. IOP Publishing, p. 012042.

Meng, L., Sabet, N., Maini, B., Dong, M., Hassanzadeh, H., 2019. Estimation of diffusion coefficient of gases in liquids from swelling data–An analytical model for including the effects of advection and density change. Fuel 252, 68-76.

Moghaddam, R.N., Rostami, B., Pourafshary, P., Fallahzadeh, Y., 2012. Quantification of density-driven natural convection for dissolution mechanism in CO_2 sequestration. Transport in porous media 92(2), 439-456.

Mohagheghian, E., Hassanzadeh, H., Chen, Z., 2019. CO2 sequestration coupled with enhanced gas recovery in shale gas reservoirs. Journal of CO2 Utilization 34, 646-655.

Moldrup, P., Olesen, T., Yoshikawa, S., Komatsu, T., Rolston, D.E.J.S.S.S.o.A.J., 2004. Three-porosity model for predicting the gas diffusion coefficient in undisturbed soil. 68(3), 750-759.

NingguangChen, ZunlongJin, YonghaoLiu, PengWang, XiaotangChen, 2020. Lattice Boltzmann simulations of droplet dynamics in two-phase separation with temperature field. Physics of Fluids 32(7), 073312.

Nojabaei, B., Johns, R.T., Chu, L.J.S.R.E., Engineering, 2013. Effect of capillary pressure on phase behavior in tight rocks and shales. 16(03), 281-289.

Odeh, A., Babu, D., 1988. Comparison of solutions of the nonlinear and linearized diffusion equations. SPE Reservoir Engineering 3(04), 1,202-201,206.

Olorode, O.M., Akkutlu, I.Y., Efendiev, Y., 2017. Compositional reservoir flow simulation for organic-rich gas shale, SPE Reservoir Simulation Conference. Society of Petroleum Engineers.

Orozco, D., Fragoso, A., Selvan, K., Noble, G., Aguilera, R.J.S.R.E., Engineering, 2020. Eagle Ford Huff 'n'Puff Gas-Injection Pilot: Comparison of Reservoir-Simulation, Material Balance, and Real Performance of the Pilot Well. 23(01), 247-260.

Ott, J.B., Boerio-Goates, J., 2000. Chemical Thermodynamics: Advanced Applications: Advanced Applications. Elsevier.

Perez, F., Devegowda, D., 2020. Molecular Signatures of Solvent Injection in Shale Organic Nanopores, SPE Improved Oil Recovery Conference. Society of Petroleum Engineers.

Rapaka, S., Chen, S., Pawar, R.J., Stauffer, P.H., Zhang, D., 2008. Non-modal growth of perturbations in density-driven convection in porous media. Journal of Fluid Mechanics 609, 285-303.

Rassenfoss, S.J.J.o.P.T., 2017. Shale EOR works, but will it make a difference? 69(10), 34-40.

Ritchie, H., Roser, M., 2016. CO_2 and GHG Emissions By Sector. Our World In Data.

Sadegh Sharafi, M., Ghasemi, M., Ahmadi, M., Kazemi, A., 2020. An experimental approach for measuring carbon dioxide diffusion coefficient in water and oil under supercritical conditions. Chinese Journal of Chemical Engineering.

Santos, T.V., Pereira, M.F., Avelino, H.M., Caetano, F.J., Fareleira, J.M., 2017. Viscosity and density measurements on liquid n-tetradecane at moderately high pressures. Fluid Phase Equilibria 453, 46-57.

Satbhai, O., Roy, S., 2020. Criteria for the onset of convection in the phase-change Rayleigh–Bénard system with moving melting-boundary. Physics of Fluids 32(6), 064107.

SCHOPPER, J.R., 1966. A theoretical investigation on the formation factor/permeability/porosity relationship using a network model. Geophysical Prospecting 14(3), 301-341.

Schopper, 1966. A theoretical investigation on the formation factor/permeability/porosity relationship using a network model. 14(3), 301-341.
Sheng, J.J., 2015. Enhanced oil recovery in shale reservoirs by gas injection. Journal of Natural Gas Science and Engineering 22, 252-259.

Siavashi, M., Talesh Bahrami, H.R., Saffari, H., 2015. Numerical investigation of flow characteristics, heat transfer and entropy generation of nanofluid flow inside

an annular pipe partially or completely filled with porous media using two-phase mixture model. Energy 93, 2451-2466.

Song, C., Yang, D., 2017. Experimental and numerical evaluation of CO2 huff-n-puff processes in Bakken formation. Fuel 190, 145-162.

Squires, T.M., Quake, S.R., 2005. Microfluidics: Fluid physics at the nanoliter scale. Reviews of Modern Physics 77(3), 977-1026.

Tan, K.-K., Sam, T., Jamaludin, H., 2003a. The onset of transient convection in bottom heated porous media. International Journal of Heat and Mass Transfer 46(15), 2857-2873.

Tan, K.-K., Sam, T., Jamaludin, H.J.I.J.o.H., Transfer, M., 2003b. The onset of transient convection in bottom heated porous media. 46(15), 2857-2873.

Thakur, G., 2019. Enhanced Recovery Technologies for Unconventional Oil Reservoirs. Journal of Petroleum Technology 71(09), 66-69.

Tran, S., Yassin, M.R., Eghbali, S., Doranehgard, M.H., Dehghanpour, H.J.S.J., 2021. Quantifying oil-recovery mechanisms during natural-gas huff 'n'puff experiments on ultratight core plugs. 26(01), 498-514.

van Duyn, C.J., Peletier, L.A., 1977. A class of similarity solutions of the nonlinear diffusion equation. Nonlinear Analysis: Theory, Methods & Applications 1(3), 223-233.

Vilarrasa, V., Bolster, D., Olivella, S., Carrera, J., 2010. Coupled hydromechanical modeling of CO2 sequestration in deep saline aquifers. International Journal of Greenhouse Gas Control 4(6), 910-919.

Vishnampet, R., Narasimhan, A., Babu, V., 2011. High Rayleigh Number Natural Convection Inside 2D Porous Enclosures Using the Lattice Boltzmann Method. Journal of Heat Transfer 133(6).

Xiong, Q., Ayani, M., Barzinjy, A.A., Dara, R.N., Shafee, A., Nguyen-Thoi, T., 2020a. Modeling of heat transfer augmentation due to complex-shaped turbulator using nanofluid. Physica A: Statistical Mechanics and its Applications 540, 122465.

Xiong, Q., Tlili, I., Dara, R.N., Shafee, A., Nguyen-Thoi, T., Rebey, A., Haq, R.-u., Li, Z., 2020b. Energy storage simulation involving NEPCM solidification in appearance of fins. Physica A: Statistical Mechanics and its Applications 544, 123566.

Yaghoubi Emami, R., Siavashi, M., Shahriari Moghaddam, G., 2018. The effect of inclination angle and hot wall configuration on Cu-water nanofluid natural convection inside a porous square cavity. Advanced Powder Technology 29(3), 519-536.

Yang, C., Gu, Y., 2006. Accelerated mass transfer of CO_2 in reservoir brine due to density-driven natural convection at high pressures and elevated temperatures. Industrial & engineering chemistry research 45(8), 2430-2436.

Yassin, M.R., 2019. Evaluation of Wettability and EOR Potential of Shale and Tight Formations, Civil and Environmental Engineering. University of Alberta, Canada.

Yassin, M.R., Habibi, A., Zolfaghari, A., Eghbali, S., Dehghanpour, H., 2018. An Experimental Study of Nonequilibrium Carbon Dioxide/Oil Interactions. SPE Journal 23(05), 1768-1783.

Yu, W., Lashgari, H.R., Wu, K., Sepehrnoori, K.J.F., 2015. CO_2 injection for enhanced oil recovery in Bakken tight oil reservoirs. 159, 354-363.

Zhang, K., Doughty, C., Wu, Y.-S., Pruess, K., 2007. Efficient parallel simulation of CO_2 geologic sequestration insaline aquifers. Ernest Orlando Lawrence Berkeley NationalLaboratory, Berkeley, CA (US).

Zhang, Y., Hyndman, C., Maini, B., 2000. Measurement of gas diffusivity in heavy oils. Journal of Petroleum Science and Engineering 25(1-2), 37-47.

Zhang, Y., Lashgari, H.R., Di, Y., Sepehrnoori, K.J.F., 2017. Capillary pressure effect on phase behavior of CO_2/hydrocarbons in unconventional reservoirs. 197, 575-582.

Zhang, Y.P., Hyndman, C.L., Maini, B.B., 2000. Measurement of gas diffusivity in heavy oils. Journal of Petroleum Science and Engineering 25(1), 37-47.

Zheng, S., Li, H.A., Sun, H., Yang, D.J.I., Research, E.C., 2016a. Determination of diffusion coefficient for alkane solvent–CO2 mixtures in heavy oil with consideration of swelling effect. 55(6), 1533-1549.

Zheng, S., Sun, H., Yang, D.J.I.J.o.H., Transfer, M., 2016b. Coupling heat and mass transfer for determining individual diffusion coefficient of a hot C3H8–CO2 mixture in heavy oil under reservoir conditions. 102, 251-263.

Zick, A., 1986. A combined condensing/vaporizing mechanism in the displacement of oil by enriched gases, SPE annual technical conference and exhibition. Society of Petroleum Engineers.

Zou, C., 2017. Chapter 1 - Introduction, in: Zou, C. (Ed.) Unconventional Petroleum Geology (Second Edition). Elsevier, pp. 3-48.

Appendices

Appendix A. Mixture velocity derivation

The mass balance equation for the oil and gas mixture (Figure 3–1) can be written as (Bird et al., 2007; Meng et al., 2019)

$$\frac{\partial(\rho\omega_s)}{\partial t} + \frac{\partial(\rho u\omega_s)}{\partial z} = -\frac{\partial}{\partial x}\left(-\rho\frac{D}{\emptyset}\frac{\partial\omega_s}{\partial z}\right) \tag{A-1}$$

For the mixture, the continuity equation is as follows:

$$\frac{\partial\rho}{\partial t} = -\frac{\partial(\rho u)}{\partial z} \tag{A-2}$$

Combining Eqs. (A-1) and (A-2), we have (James et al., 2012; Meng et al., 2019)

$$\rho\frac{\partial\omega_s}{\partial t} + \rho u\frac{\partial\omega_s}{\partial z} = \frac{\partial}{\partial x}\left(\rho\frac{D}{\emptyset}\frac{\partial\omega_s}{\partial z}\right) \tag{A-3}$$

Dividing Eq. (A-3) by $\frac{\rho\partial\omega_s}{\partial\rho}$, yields

$$\frac{\partial u}{\partial z} = -\frac{1}{\rho^2}\frac{\partial\rho}{\partial\omega_s}\frac{\partial}{\partial z}\left(\rho\frac{D}{\emptyset}\frac{\partial\omega_s}{\partial z}\right) \tag{A-4}$$

Integration of Eq. (A-4) from $-\infty$ to z, we have (Meng et al., 2019):

$$u = \frac{(\rho_o-\rho_s)}{\rho_s\rho_o}\int_{-\infty}^{z}d\left(\rho\frac{D}{\emptyset}\frac{\partial\omega_s}{\partial z}\right) = \frac{(\rho_o-\rho_s)}{\rho_s\rho_o}[\rho\frac{D}{\emptyset}\frac{\partial\omega_s}{\partial z}\big|_z - \rho\frac{D}{\emptyset}\frac{\partial\omega_s}{\partial z}\big|_{-\infty}] \tag{A-5}$$

According to Eq. (3-6), $\frac{\partial\omega_s}{\partial z}\big|_{-\infty} = 0$, therefore the mixture velocity is written as (James et al., 2012; Meng et al., 2019)

$$u = \frac{(\rho_o-\rho_s)}{\rho_s\rho_o}\rho\frac{D}{\emptyset}\frac{\partial\omega_s}{\partial z} \tag{A-6}$$

Appendix B. Derivation of ω_s equation

$$\frac{\partial \omega_s}{\partial t} = \frac{D}{\emptyset} [\frac{\partial^2 \omega_s}{\partial z^2} + 2 \left(\frac{\partial \omega_s}{\partial z}\right)^2 \frac{(\rho_s - \rho_o)}{\rho_s + \omega_s(\rho_o - \rho_s)}]$$

(B-1)

Eq. (B-1) is nonlinear; therefore, we linearize it using the following transform (Meng et al., 2019; Odeh and Babu, 1988):

$$n = \frac{1}{1 + \omega_s \alpha}$$

(B-2)

Using Eq. (B-2), Eq. (B-1) becomes (Meng et al., 2019):

$$\frac{\partial n}{\partial t} = \frac{D}{\emptyset} \frac{\partial^2 n}{\partial z^2}$$

(B-3)

The new initial and boundary conditions for Eq. (B-3) are as follows:

$$\begin{cases} n\,(z,\ t = 0) = 1 \\ \\ n\,(z = 0,\ t) = \dfrac{1}{1 + \omega_{so} \alpha} \\ \\ \dfrac{\partial n\,(z \to -\infty,\ t)}{\partial z} = 1 \end{cases}$$

(B-4)

To solve Eq. (C-3), we use the following similarity variable (Meng et al., 2019; van Duyn and Peletier, 1977):

$$\eta = \frac{z}{2\sqrt{\frac{D}{\emptyset} t}}$$

(B-5)

Using η, Eq. (B-3) can be written as follows (Meng et al., 2019):

$$\frac{\partial^2 n}{\partial \eta^2} + \eta \frac{\partial n}{\partial \eta} = 0$$

(B-6)

The new initial and boundary conditions are:

$$n\,(\eta \to \infty) = 1 \tag{B-7}$$

$$\begin{cases} n\,(\eta \to \infty) = 1 \\ \\ n\,(\eta \to -\infty) = \dfrac{1}{1 + \omega_{so}\alpha} \\ \\ \dfrac{\partial n\,(\eta \to 0)}{\partial z} = 1 \end{cases}$$

Solving Eq. (B-6) with the above initial and boundary conditions yields (Meng et al., 2019):

$$\omega_s = \frac{1}{\alpha}\left(\left[1 - \frac{\alpha\omega_{s0}}{1 + \alpha\omega_{s0}}\,erfc\left(-\frac{z}{2\sqrt{\dfrac{D}{\varnothing}\,t}}\right)\right]^{-1} - 1\right) \tag{B-8}$$

Appendix C. Derivation of the diffusion coefficient

Using Darcy velocity (q), the continuity equation for the mixture can be written as:

$$-\frac{d(\rho q)}{dz} = \frac{d(\rho\varnothing)}{dt} \tag{C-1}$$

Considering the constant porosity ($C_\varnothing = 0$), the right-hand side of the (C-1) equation can be written as:

$$\frac{d(\rho\varnothing)}{dt} = \varnothing\frac{d\rho}{dp}\frac{dp}{dt} = \rho\,\varnothing\,C_f\frac{dp}{dt} \tag{C-2}$$

Here, C_f is the fluid compressibility and defines as $C_f = \frac{1}{\rho}\frac{d\rho}{dp}$. Using Darcy law, the LHS of Eq. (C-1) can be written as:

$$-\frac{d(\rho q)}{dz} = \frac{\rho k}{\mu}\left[\frac{d^2 p}{dz^2} + C_f\left(\frac{dp}{dz}\right)^2\right] \tag{C-3}$$

Equating Eqs. (C-2) and (C-3) yields:

$$\frac{d^2p}{dz^2} + C_f \left(\frac{dp}{dz}\right)^2 = \frac{\emptyset \, \mu \, C_f}{k} \frac{dp}{dt} \tag{C-4}$$

From Eq. (3-8) and Darcy law at the core's surface (z=0), we have:

$$\begin{cases} \dfrac{dp}{dz} = \dfrac{k\sqrt{\emptyset D}\, \alpha\, \omega_{s0}}{\mu\sqrt{\pi t}} \\[2mm] \dfrac{d^2p}{dz^2} = 0 \end{cases} \tag{C-5}$$

Substituting Eq. (C-5) into Eq. (C-4) and rearrangement, we have (at z=0):

$$D\frac{dt}{t} = \frac{k\,\pi\,t}{\omega_{s0}{}^2\alpha^2\,\mu}\,dp \tag{C-6}$$

Integrating from both sides of Eq. (C-6), the diffusion coefficient can be calculated as:

$$D = \frac{k\,\pi}{\omega_{s0}{}^2\alpha^2\,\mu}\,\frac{(p-p_{eq})}{\ln\left(\frac{t_{eq}}{t}\right)} \tag{C-7}$$

Appendix D. Derivation of oil production in Eq. (3-11)

Starting from Eq. (3-10), we have:

$$\int_0^t \emptyset\,\rho\,u\,A\,dt = m \tag{D-1}$$

Substituting Eqs. (3-3) and (3-4) into Eq. (D-1), yields:

$$\int_0^t \frac{1}{(1+\omega_s\,\alpha)^2}\,\frac{\partial \omega_s}{\partial x}\,dt = \frac{m}{A\alpha D\,\rho_o} \tag{D-2}$$

Considering $\dfrac{\partial \omega_s}{\partial x} = \dfrac{\partial \omega_s}{\partial n}\dfrac{\partial n}{\partial \eta}\dfrac{\partial \eta}{\partial x}$ and using Eq. (B-2), Eq. (D-2) can be written as follows:

$$\int_0^t n^2\frac{1}{\alpha}\,\frac{1}{n^2}\frac{2}{\sqrt{\pi}}\frac{a\omega_{s0}}{1+a\omega_{s0}}\frac{1}{2\sqrt{\frac{D}{\emptyset}t}}\,dt = \frac{m}{A\alpha D\,\rho_o} \tag{D-3}$$

Taking integral from Eq. (D-3) and doing some simplifications, we have:

$$m = \frac{2A\sqrt{D\emptyset}\rho_o\sqrt{t}}{\sqrt{\pi}}\left(\frac{\omega_{s0}\,\alpha}{1 + \omega_{s0}\,\alpha}\right) \tag{D-4}$$